Zeitschrift: Helvetica Physica Acta

Band: 68 (1995)

Heft: 2

Vereinsnachrichten: Réunion de printemps de la Société Suisse de Physique = Frühjahrstagung der Schweizerischen Physikalischen Gesellschaft = Spring meeting of the Swiss Physical Society

Autor: [s.n.]

Nutzungsbedingungen

Die ETH-Bibliothek ist die Anbieterin der digitalisierten Zeitschriften auf E-Periodica. Sie besitzt keine Urheberrechte an den Zeitschriften und ist nicht verantwortlich für deren Inhalte. Die Rechte liegen in der Regel bei den Herausgebern beziehungsweise den externen Rechteinhabern. Das Veröffentlichen von Bildern in Print- und Online-Publikationen sowie auf Social Media-Kanälen oder Webseiten ist nur mit vorheriger Genehmigung der Rechteinhaber erlaubt. Mehr erfahren

Conditions d'utilisation

L'ETH Library est le fournisseur des revues numérisées. Elle ne détient aucun droit d'auteur sur les revues et n'est pas responsable de leur contenu. En règle générale, les droits sont détenus par les éditeurs ou les détenteurs de droits externes. La reproduction d'images dans des publications imprimées ou en ligne ainsi que sur des canaux de médias sociaux ou des sites web n'est autorisée qu'avec l'accord préalable des détenteurs des droits. En savoir plus

Terms of use

The ETH Library is the provider of the digitised journals. It does not own any copyrights to the journals and is not responsible for their content. The rights usually lie with the publishers or the external rights holders. Publishing images in print and online publications, as well as on social media channels or websites, is only permitted with the prior consent of the rights holders. Find out more

Download PDF: 10.12.2025

ETH-Bibliothek Zürich, E-Periodica, https://www.e-periodica.ch

Réunion de Printemps de la Société Suisse de Physique

Frühjahrstagung der Schweizerischen Physikalischen Gesellschaft

Spring Meeting of the Swiss Physical Society

March 23 and 24, 1995

Bern, Switzerland

Helv Phys Acta
Vol. 68 (1995)

0018-0238/95/020191-02$1.50+0.20/0
(c) Birkhäuser Verlag, Basel

A new view on the particle description in Quantum Field Theory

E. Frochaux

Département de Mathématiques,
Ecole Polytechnique Fédérale, CH-1015 Lausanne, Switzerland

It is generally admitted that particles in Quantum Field Theory can only be defined in an asymptotic way. Thus the bound states, for instance, could only be obtained from the scattering theory, in which they appear as single particles, that is without conveying information on their internal structure.

But particles can also be seen in the spectrum of the mass operator M. Each bound state mass is an eigenvalue of M, and the corresponding eigenspace carries all available information on its internal structure.

In a bosonic model of QFT in two space-time dimensions, with weak coupling, in which a bound state is known to exist, a family of vector states Ψ_f has been constructed, parametrized linearly by functions $f(p_1, p_2)$ of two momenta, which satisfies

$$m_B^2 = \inf_{0 \neq f \in \Gamma} \frac{(\Psi_f; M^2 \Psi_f)}{\|\Psi_f\|^2} + O(\lambda^N)$$

where m_B is the bound state mass, λ is the coupling constant and Γ is a ball of a Banach space on which the N-order perturbation remainder is uniformly bounded. Ψ_f appears to be the N-order approximation of an eigenvector. The calculation of the infimum of the above quotient of bilinear forms leads to the eigenvalue equation

$$\mathcal{M}_0(p)^2 f(p) + \int d\sigma(p') f(p') K(p, p') \delta(p_1 + p_2 - p_1' - p_2') = (m_B^2 + O(\lambda^N)) f(p)$$

where $d\sigma$ is the Lorentz-invariant measure, $\mathcal{M}_0$ is the mass kernel of the free model ($d\sigma$ and $\mathcal{M}_0$ are written with the renormalized one-particle mass) and K, the non-local interaction kernel, is calculated at first perturbation orders. At first order K coincides with the Bethe-Salpeter kernel on mass shell, but without the condition $\omega(p_1) + \omega(p_2) = \omega(p_1') + \omega(p_2')$. At second order it differs from the B.S. kernel.

This equation should play the role of a 'relativistic Schrödinger equation'. To get a better understanding of the situation we calculate

$$\frac{(\Psi_f; P\Psi_f)}{\|\Psi_f\|^2}\ ; \quad \frac{(\Psi_f; H\Psi_f)}{\|\Psi_f\|^2}\ ; \quad \frac{(\Psi_f; L\Psi_f)}{\|\Psi_f\|^2}$$

where P is the total momentum, H the Hamiltonian and L the generator of the Lorentz transformations. We get three quotients of bilinear forms for f. Operators which generate these forms can be collected in a nice theory as follows.

Let $\mathcal{H}$ be the Hilbert space $L^2(\mathbb{R}^2, d\sigma)$ with the measure $d\sigma(p) = [4\omega(p_1)\omega(p_2)]^{-1}\, dp_1 dp_2$, where $\omega(p_i) = (p_i^2 + m^2)^{1/2}$ and m is the renormalized one-particle mass. We consider on $\mathcal{H}$ the unbounded (but self-adjoint) operators

$$\begin{aligned} Pf(p) &= (p_1 + p_2)f(p) \\ H_0 f(p) &= (\omega(p_1) + \omega(p_2))f(p) \\ L_0 f(p) &= -i(\omega(p_1)\partial_{p_1} + \omega(p_2)\partial_{p_2})f(p). \end{aligned}$$

Let $\mathcal{O}$ be the following 'interaction operator'

$$\mathcal{O}f(p) = \int d\sigma(p')f(p')\frac{K(p,p')\ \delta(p_1 + p_2 - p_1' - p_2')}{\omega(p_1) + \omega(p_2) + \omega(p_1') + \omega(p_2')}$$

where K is the previous kernel. The operators of the 'interaction case' :

$$\begin{aligned} P &\ \ as\ \ before \\ H &= H_0 + H_0\mathcal{O} + \mathcal{O}H_0 \\ L &= L_0 + L_0\mathcal{O} + \mathcal{O}L_0 \end{aligned}$$

can be well defined and they satisfy the commutation rules of the Poincaré algebra

$$\begin{aligned} [P, H] &= 0 \\ [P, L] &= iH \\ [H, L] &= iP \end{aligned}$$

the last one being satisfied only up to $O(\lambda^N)$.

Instead of calculating the next orders (which is extremely long) it is tempting to try to solve directly the commutation rules, even if we may leave QFT. So we consider now K as unknown and check the commutation rules. We suppose that K and L_0K are continuous and bounded (which seems to hold in QFT). The two first commutation rules are automatically satisfied for all K (because of the δ function in $\mathcal{O}$). The last one gives an integro-differential non-linear equation for K.

By the Banach fixed-point theorem in the Banach space for the norm

$$|K| = \sup_{p_1, p_2, p_1'} \{|K(p,p')| + |L_0K(p,p')|\}_{p_2' = p_1 + p_2 - p_1'}$$

this equation can be solved. More precisely we get the complete set of solutions lying in the ball $|K| < m^2/16$, and they are given by convergent series involving arbitrary functions, which represent nothing else than the kernel K in the centre-of-mass frame, that is $K(p_1, p_2, p_1', p_2')$ for $p_1 + p_2 = p_1' + p_2' = 0$. If such a solution effectively holds in these QFT model, a complete and precise description of interacting particles would be available for the first time in a QFT framework.

References

E. Frochaux, Helv. Phys. Acta 61, p. 923-957 (1988); Nucl. Phys. B 389, p. 666-702 (1993); Helv. Phys. Acta 68 p. 47-63 (1995).

Helv Phys Acta
Vol. 68 (1995)

0018-0238/95/020193-02$1.50+0.20/0
(c) Birkhäuser Verlag, Basel

Inverse orbits for spin systems

V. Bochicchio, J.J. Loeffel

Institute of Theoretical Physics, University of Lausanne, CH-1015 Lausanne

Abstract For the mathematics of equilibrium statistical mechanics, spin systems on a arbitrary lattice (such as the familiar Ising model) are equivalent to highly inhomogeneous spin systems on the half line $\mathbb{N}$. For a system of this latter class, we explain how to reduce the problem of finding all the Gibbs measures compatible with given neighbor potential U (the **Dobrushin-Lanford-Ruelle** problem) to the problem of finding suitable "inverse orbits" of a certain "inverse" dynamical system, which happens to be non autonomous but linear. As an illustration, we give a result concerning the number of extreme points of $\mathcal{G}(U)$, the set of all Gibbs measures for the potential U.

A detailed formulation of the Dobrushin-Lanford-Ruelle (DLR) problem for general spin systems on a lattice with given neighbor potential may be found in several papers, see for example [Loeffel (90)] and [Griffeath (76)], or in general texbooks [Georgii (88)] so that only a brief statement of this problem is reported here. Further, following an idea exposed in [Griffeath (76) pp 436] any spin systems with given neighbor potential may be regard as a spin system on the half line $\mathbb{N}$. Thus, from now on, only spin sytems of this latter class will be considered here.

Given a family $S = \{S_n\}_{n\in\mathbb{N}}$ of finite sets, S_n being the set of "spin states" at the site n, a configuration of the infinite system is described by an element $\omega \in \Omega = \Pi_{n\in\mathbb{N}} S_n$; Ω is equipped with the usual product σ-algebra $\mathcal{F}$. A neighbor potential on $\mathbb{N}$ is a family $U = \{(J_n, h_n)\}_{n\in\mathbb{N}}$ of real valued functions where $J_n : S_n \times S_{n+1} \to \mathbb{R}$, $h_n : S_n \to \mathbb{R}$; from this potential one can define a family of local conditional probabilities called a specification in [Loeffel (90)] and [Georgii (88), chap.2] or the local characteristics in [Griffeath (76)]. Then, the DLR problem consists in finding all Markov fields on $(\Omega, \mathcal{F})$ whose local conditional expectations coincide with the local conditional probabilities specified by U. The set $\mathcal{G}(U)$ of all such probability measures forms a non-empty compact simplex of $\mathcal{P}(\Omega, \mathcal{F})$, the set of all probability measures on $(\Omega, \mathcal{F})$.

In view to study the abstract set $\mathcal{G}(U)$ under a more geometrical point of view, we introduce now the notion of **positive normalized inverse orbits** :
Let $A = \{A_n\}_{n\in\mathbb{N}}$ be a family of matrices $A_n : S_n \times S_{n+1} \to \mathbb{R}_{>0}$ defined from U by putting

$$A_n(\sigma, \rho) = \exp -(h_n(\sigma) + J_n(\sigma, \rho)) > 0. \tag{1}$$

If $T_n = \mathbb{R}^{S_n}$ denotes the real vector space of functions $S_n \to \mathbb{R}$, it will often be convenient to interpret A_n as a linear mapping $A_n : T_{n+1} \to T_n$ defined by

$$A_n f_{n+1}(\sigma) = \sum_{\rho\in S_{n+1}} A_n(\sigma, \rho) f_{n+1}(\rho). \tag{2}$$

Then, a family $f = \{f_n\}_{n\in\mathbb{N}}$ belonging to the infinite vector space product $\mathcal{U} = \Pi_{n\in\mathbb{N}} T_n$ is called **a positive normalized inverse orbite** relative to A if $f_n(\rho) \geq 0$, $\sum_{\sigma\in S_0} f_0(\sigma) = 1$, and

$$f_n = A_n f_{n+1} \tag{3}$$

for all $n \in \mathbb{N}, \rho \in S_n$. Using mainly geometrical considerations it can be proved that $\mathcal{O}_{+,norm}(A)$, the set of all such families, is a non-empty compact simplex of $\mathcal{U}$.

The interest in studying $\mathcal{O}_{+,norm}(A)$ for the investigation of $\mathcal{G}(U)$ lies in the following result: the map $\mathcal{O}_{norm,+}(A) \to \mathcal{G}(U)$, $f \mapsto \mu$ given by

$$\mu(\{\nu \in \Omega : \nu_{[0,n]} = \omega_{[0,n]}\}) = A_0(\omega_0, \omega_1)...A_{n-1}(\omega_{n-1}, \omega_n) f_n(\omega_n) \tag{4}$$

for all finite cylinder sets based on $\omega_{[0,n]}$, is an affine bijection. Thus, the DLR problem for spin systems with given neighbor potential may be reduced to the more geometrical and intuitive problem of finding suitable families of columns vectors satisfying the linear "inverse" dynamical system expressed in (3).

As an illustration, let us give one of the many results concerning $\mathcal{G}(U)$ that can be obtained geometrically using the theory of positive normalized inverse orbits : for their special mathematical properties and their physical interpretation, the most interesting elements of the convex set $\mathcal{G}(U)$ are its extreme points (see for example [Georgii (88) pp 119] and [Winkler (81)]). If $\mathcal{E}(U)$ denotes the set of these extreme points it can be proved, assuming that $\mathcal{E}(U)$ is finte, that

$$1 \leq \mid \mathcal{E}(U) \mid \leq \liminf_{n\to\infty} \text{ rank } A_n \leq \liminf_{n\to\infty} \mid S_n \mid . \tag{5}$$

Bibliographic notes and references:

Similar objects to the exposed positive normalized inverse orbits appear in [Georgii (88) pp 213] under the name of "entrance laws"; in [Griffeath (76)] the term of "non-negative normalized P-regular functions" is used while [Winkler (81)] called these objects "harmonic functions".

1. J.J Loeffel (90): About Gibbs states on Bethe lattices in: S. Albeverio, G.Casati, U.Cattaneo, D.Merlini and R. Moresi (eds). Proceedings of a conference in Ascona in July 88 on *Stochastic processes, physics and geometry* pp 497-515. Singapore, New Jersey, London, Hong Kong : World Scientific.

2. H.O. Georgii (88): *Gibbs measures and phase transition.* Berlin, Walter de Gruyter.

3. D. Griffeath (76): Introduction to random fields. Chap.12, pp 425-458 in: J.G. Kemeny, J.L. Snell and A.W. Knapp, *Denumerable Markov chains*, 2nd ed. New York, Springer.

4. G.Winkler (81): The Number of Phases of Inhomogeneous Markov Fields with Finite State Spaces on $\mathbb{N}$ and $\mathbb{Z}$ and their Behaviour at Infinity in Math. Nachr. 104, pp 101-117.

Helv Phys Acta
Vol. 68 (1995)

0018-0238/95/020195-02$1.50+0.20/0
(c) Birkhäuser Verlag, Basel

Light Confinement by Subwavelength Objects in Near–Field Optics

O.J.F. Martin[1], C. Girard[2] and A. Dereux[3]

[1] Institut für Feldtheorie, ETH-Zentrum, CH-8092 Zurich, Switzerland
[2] Lab. Physique Moléculaire, UA CNRS 772, 25030 Besançon, France
[3] ISIS, Fac. Univ. Notre–Dame de la Paix, 5000 Namur, Belgium

We show that dielectric objects much smaller than the wavelength used to illuminate them, can produce a confined electric field that perfectly reproduces their shape. This field can be recorded by a scanning near–field optical microscope (SNOM), which explains how these devices reach a resolution far beyond the diffraction limit.

Among the different theoretical problems raised by the recent developments of SNOM [1], the extraordinary resolution achieved by this new type of microscope is one of the most fascinating [2]. To investigate this question, we consider the scattering by a subwavelength hollow dielectric object (Fig. 1) and use the generalized field propagator [3] to compute the electric field in an observation plane located at a distance d from the scatterer (Fig. 1). The field in this plane corresponds to the field that would be recorded by a SNOM probing tip scanning the object at a constant height.

We report in Fig. 2 the total field intensity at different observation distances, for both transverse electric (TE) and transverse magnetic (TM) polarizations. For TE polarization, when the observation distance is extremely small, strong field gradients appear along the object sides that are orthogonal to the incident electric field (Fig. 2(a)). Thus different sides of the object are enhanced, depending on the orientation of the incident field. For TM polarization, we observe a very strong field confinement that perfectly reproduces the object shape (Fig. 2(b)). Furthermore, the image does not depend on the orientation of the incident field, and the field pattern always reproduce the object shape. This behavior can be explained by depolarization effects in the scatterer [3]. Note that for TM field, the hollow in the scatterer is also perfectly resolved (Fig. 2(b)). This is not anymore the case when the observation distance increases, although a field confinement is still observed (Fig. 2(d)).

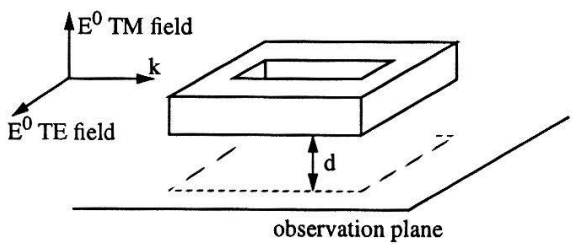

Figure 1: Geometry used for the calculation. The object is $60 \times 60 \times 10$[nm], the hollow $20 \times 20 \times 10$[nm], the dielectric constant 2.25 and the surrounding medium vacuum. The object is illuminated by a plane wave with a propagation vector $\mathbf{k}$, an incident electric field $\mathbf{E}^0$ and a wavelength 633[nm].

When the observation distance becomes larger, the scattering field tends to reproduce the radiation pattern of a dipole for both polarizations (Figs. 2(e) and 2(f)). Note that in the TM case, a peak appears just above the object, whereas in the TE case, this peak appears ahead of the object. The confinement effects observed in the near–field explain how objects much smaller than the wavelength can be resolved with a SNOM.

1. "Near–field optics," D.W. Pohl and D. Courjon, Eds. (Kluwer, Dordrecht, 1993).
2. F. Zenhausern *et al.* Appl. Phys. Lett. **65**, 1623 (1994).
3. O.J.F. Martin, C. Girard and A. Dereux, Phys. Rev. Lett. **74**, 526 (1995).

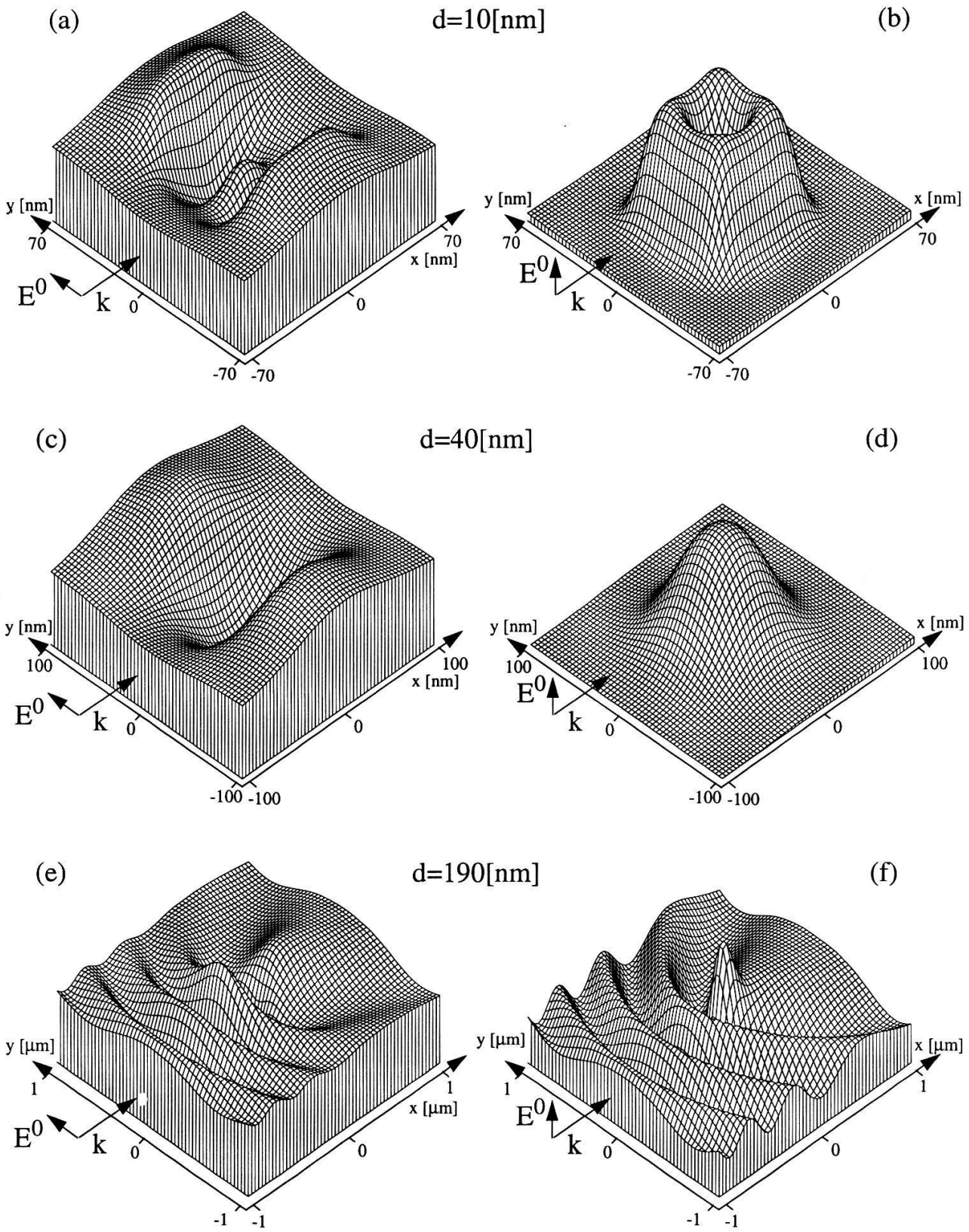

Figure 2: Field intensity in an observation plane located at a distance d from the scattering system depicted in Fig. 1. (a), (c), (e) TE incident field; (b),(d),(f) TM incident field. As the observation distance increases, the light confinement effect disappears.

Helv Phys Acta
Vol. 68 (1995)

0018-0238/95/020197-02$1.50+0.20/0
(c) Birkhäuser Verlag, Basel

Existence of d-wave and s-wave solutions of Eliashberg equations

G. Santi, T. Jarlborg and M. Peter

DPMC, University of Geneva, 1211 Geneva 4, Switzerland

We solve the Eliashberg equations for different models of electron-phonon coupling. In particular we study a coupling which is different on different parts of the Fermi surface in order to look for possible conditions for d-wave pairing. This is of some importance since many recent experiments claim d-wave pairing in YBCO. We find that a very localized interaction (i.e. a strong coupling within certain Fermi surface pieces, but weak coupling between different pieces) together with a Coulomb repulsion is favorable for d-wave pairing. The connection between the models and the calculated coupling and Fermi surface of real copper oxide systems is discussed.

There is experimental evidence for d-wave pairing symmetry in high-T_c cuprates [1], and many other features are not BCS-like in these compounds. It is usually considered that a phonon-mediated interaction can only lead to s-wave symmetry of the gap parameter [2]. Nevertheless, in this paper, we show that some of the "non-BCS" features, as d-wave pairing symmetry, can be obtained from Eliashberg equations by choosing suitable parameters for the electron-phonon coupling and the Coulomb repulsion.

We solve self-consistently the "renormalized" Eliashberg equations. This is a set of 3 coupled non-linear equations [3]. The equation for the gap parameter Φ (corresponding to the BCS gap equation) can be written, in the Matsubara representation ($\omega_n = (2n+1)\pi T$)

$$\Phi(\mathbf{k}, i\omega_n) = T \sum_{n'} \iint d^2\mathbf{k}' G(\mathbf{k}', i\omega_{n'})[D(\mathbf{k}, \mathbf{k}', i\omega_n - i\omega_{n'}) - \mu(\mathbf{k}, \mathbf{k}')]\Phi(\mathbf{k}', i\omega_{n'}) \qquad (1)$$

where G is the renormalized electronic Green function, D is the phononic interaction kernel and μ represents the Coulomb potential.

Calculations and measurements describe the Fermi surface (FS) as 2-dimensional in the cuprates. Here we separate the momentum $\mathbf{k} = (q, k)$ in parallel (q) and perpendicular (k) components with respect to the FS. We divide the FS in several pieces (q), and we set the coupling parameters in such a way that the interaction is highly attractive (due to D) for electrons belonging to the same piece, and weakly repulsive (due to μ) between most remote pieces. This kind of interaction should be favorable to d-wave pairing. In previous works, we considered a strong k-dependence of the interaction, in particular a cutoff in $|k - k'|$ (i.e. the coupling falls to zero if $|k - k'| > \xi$), and we showed that this could explain some deviations from the BCS behaviour as the diminution of the isotopic effect and the decrease of the Hebel-Slichter peak [3].

The present calculations were done with and without the cutoff. We find that a d-wave solution is possible in both cases. The d-wave solution is obtained for a coupling which is strong only when q and q' are close to each other. However, the initial condition of the iterative procedure is important. Starting with s-like gap symmetry with the same coupling

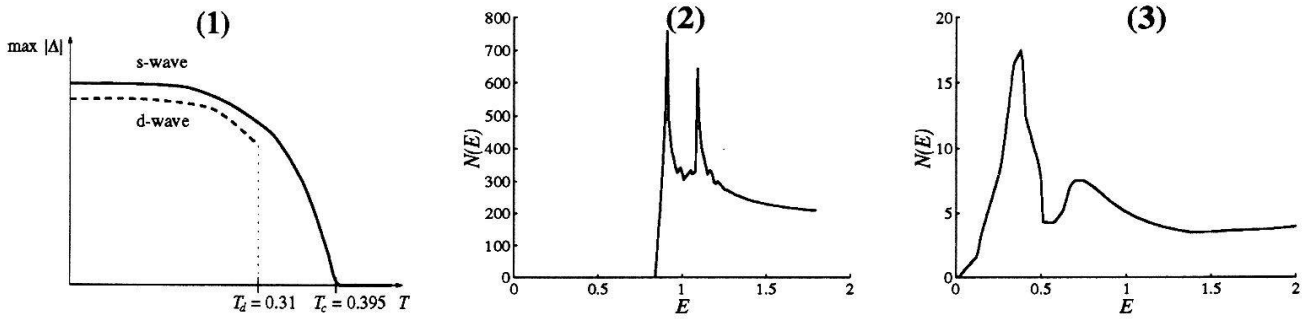

(1) Temperature dependence of the maximum of the gap Δ (being the renormalized Φ). **(2)** Density of states (DOS) for a case without cutoff, 12 FS pieces and s-wave solution. **(3)** DOS for a case with cutoff, 3 FS pieces and d-wave solution. (All energies are in units of the typical phonon frequency, and the DOS is calculated through an approximation valid for low energies).

parameters gives an s-solution. Below the temperature T_d, both solutions can exist, whereas above T_d, only the s-wave solution exists (Fig.1). Free energies are not calculated, but the d-wave might be metastable for temperatures lower than T_d, since the gap is smaller for the d-wave than for the s-wave. If the parameters are changed to a strong coupling between different q-pieces, the gap converges always to the s-wave, even if the initial condition has d-wave symmetry.

Recent experimental works on cuprates by photoemission and tunneling [5] show a second attenuated peak in the density of states. A similar behavior is found from the anisotropic s-wave solution of Eliashberg equation (Fig. 2) where 1/6 of the FS pieces have strong and the rest have weak coupling. The sharpness of the peaks is due to our neglect of lifetime effects. A different calculation with a cutoff gives a similar, second peak (Fig. 3). In the first case, the 2 peaks are due to the fact that there are mainly 2 different values of the gap, whereas in the second, they are due to the k-dependence of the energy of the quasiparticles created by the cutoff. In this case, the so-called "in-gap" states come from the d-wave symmetry.

The Eliashberg equations have a richness of solution that has still to be explored. We have shown here that some aspects of high-T_c can be accounted for with this theory. It is then premature to eliminate phonon-based mechanism to explain high-T_c superconductivity.

We wish to acknowledge M. Weger and B. Barbiellini for stimulating discussions and for their contributions at earlier stages of this work.

References

[1] D.A. Brawner and H.R. Ott, Phys. Rev. B **50**, 6530 (1994); A. Mattai, Y. Gim, R.C. Black,, A. Amar, F.C. Wellstood, preprint (1994)

[2] R. Combescot, Phys. Rev. Lett. **67**, 148 (1991)

[3] M. Weger, B. Barbiellini, T. Jarlborg, M. Peter and G. Santi, Ann. der Phys., in press (1995); M. Weger, B. Barbiellini and M. Peter, Z. Phys. B **94**, 387 (1994)

[4] G. Santi, T. Jarlborg, M. Peter and M. Weger, J. Supercond., in press (1995)

[5] Z.-X. Shen et al, Phys. Rev. Lett. **70**, 1553 (1993); D. Mandrus, J. Hartge, C. Kendziora, L. Mihaly and L. Forro, Europhys. Lett. **22**, 199 (1993); Ch. Renner and Ø. Fischer, to appear in Phys. Rev. B **51** (1995)

Helv Phys Acta
Vol. 68 (1995)

0018-0238/95/020199-02$1.50+0.20/0
(c) Birkhäuser Verlag, Basel

MD-Simulations of Scanning Force Microscopy on Self-Assembled Monolayers

T. Bonner, A. Baratoff, and H.-J. Güntherodt

Institute of Physics, University of Basel, 4056 Basel, Switzerland

We have performed molecular dynamics simulations of Scanning Force Microscopy on a Self-Assembled Monolayer (SAM), namely $S(CH_2)_{n-1}CH_3$, chemisorbed on Au(111). The probing is represented by a pyramid of atoms connected via three orthogonal springs to a rigid support. The latter is slowly approached towards the sample and then scanned over several unit cells of the underlying $\sqrt{3}\times\sqrt{3}$ S-lattice at constant velocity. Atomic-scale corrugation and stick-slip events (mainly determined by CH_3 tail groups) are observed in the normal and lateral movements of the sensing tip together with accompanying changes in the SAM.

Self-assembled monolayers (SAMs), in particular alkyl-thiolates chemisorbed from solution on Au(111), have been intensively investigated over the past few years [3]. On one hand they have important applications as inert wear and corrosion-resistant coatings or as micropatterned functionalized substrates for biomolecules or sensors [2]. On the other hand, as compact carpet-like ultrathin films of firmly anchored, though flexible molecules with nontrivial internal degrees of freedom, they represent a fruitful area for fundamental experimental and theoretical investigations.

To understand scanning force microscopy with molecular resolution on such systems, in particular mechanisms of friction, we have performed molecular dynamics simulations on arrays of inert $CH_3(CH_2)_{n-1}S$ molecular chains adsorbed on Au(111) for n=5 to 11 at various temperatures. As in previous simulations on free n=16 SAMs [5], bond length are constrained to be constant, and methyl and methylene groups are represented as 'united atoms' in order to eliminate fast, but small-amplitude stretching vibrations. Interactions with the substrate (and with the probing tip, if present), as well as between molecules are represented by potentials of the Lennard-Jones type smoothly cut off beyond 12 Å. The same applies to atoms within each molecule beyond fourth neighbors, while closer neighbors are coupled by parametrized bond-bending and torsional potentials. The chemisorbed sulfurs are subject to a sinusoidal potential commensurate with the substrate. In agreement with previous simulations, with increasing temperature a free monolayer passes through different phases where the molecules are successively ordered in a honeycomb pattern, rotate about a common tilt axis, precess about the substrate normal, and finally untilt as thermally activated gauche defects preferrentially appear near the methyl end groups [5]. At a given temperature we find a similar behavior with decreasing n, as expected from the reduced intermolecular interactions. Although this model fails to reproduce the observed superstructures [6, 1, 4] and precise interlocking between neighboring molecules [4], it adequately represents their packing and $\approx 30°$ tilt away from the surface normal.

The probing tip and cantilever of a scanning force microscope are represented by a single atom or a pyramidal cluster connected by orthogonal springs to a rigid support. The latter

is approached an then scanned over several unit cells of the underlying $\sqrt{3} \times \sqrt{3}R30°$ sulfur adlattice at constant distance and velocity (variable deflection mode). Test runs reveal the overall force-distance characteristics at different positions. They can be used to judge wether perpendicular or lateral mechanical instabilities might occur and thus to choose parameters for subsequent fully dynamical runs corresponding to the possible regimes described below. Care is then taken to separation of relevant time scales (scanning, instrument response, SAM evolution). Damping or, preferrably averaging or filtering, representing the finite bandwidth of the detection electronics, can be introduced to reduce the instrument response to rapid SAM motions and to oscillations excited by mechanical instabilities. Molecular-scale corrugation, mainly determined by the methyl end groups, and slow motions withing the SAM, can be continuously followed in perpendicular and transverse deflections for sufficiently weak loads and stiff springs. Otherwise 3D stick-slip occurs, leading to net friction, either extrinsic, i.e. governed by the soft spring constant(s) of the instrument, or intrinsic, i.e. more affected by the sample itself. In the latter case, the simulated array, comparable in size to an ordered SAM domain at room temperature [6, 1], is collectively tilted towards the scan direction. Although this 'combing' effect already occurs with a single-atom tip in weak (0.1 nN) repulsive contact, the tip must be represented by a cluster at higher loads resulting in partial penetration and irregular stick-slip events. Similar nanoinstabilities, due to particular molecules being strongly deformed close to the tip, lead to fine structure in perpendicular force-displacement characteristics.

In view of the relative complexity of the systems studied, it is instructive to visualize their time evolution by means of video sequences generated from compressed data. This capability provides a useful global overview of phenomena (and possible artifacts) which occur in a given simulation, thus facilitating decisions concerning future runs. In conclusion, our results provide insights into the molecular origin of friction and viscoelastic response in systems representative of organic soft matter, which are also well-characterized and both fundamentally interesting and promising for applications on their own.

References

[1] D. Anselmetti, A. Baratoff, H.-J. Güntherodt, E. Delamarche, B. Michel, Ch. Gerber, H. Kang, H. Wolf, and H. Ringsdorf, Europhysics Lett. **27**, 365 (1994).

[2] A. Kumar and G.M. Whitesides, Science **263**, 60 (1994).

[3] A. Ulman, *An Introduction to Ultrathin Organic Films* Academic Press, New York (1991).

[4] P. Fenter et al., Science **266**, 1216 (1995).

[5] J. Hautman and M.J. Klein, J. Chem. Phys. **93**, 7483 (1990).

[6] N. Camillone III et al., J. Chem. Phys. **99**, 744 (1993).

Helv Phys Acta
Vol. 68 (1995)

0018-0238/95/020201-02$1.50+0.20/0
(c) Birkhäuser Verlag, Basel

SPIN FILTER EFFECT IN Co/Cu(100): THICKNESS DEPENDENT PHOTOELECTRON SPIN POLARIZATION

D. OBERLI, J.C. GRÖBLI and F. MEIER
Laboratorium für Festkörperphysik, ETH-Hönggerberg, CH-8093 Zürich

At photothreshold the spin polarization of the photoelectrons emitted from cesiated Co films evaporated on Cu(100) changes sign depending on the thickness of the Co film: For thin Co films (d<27Å) a negative polarization at the threshold is measured whereas for thicker Co films a positive polarization is found. These observations can be understood with a spin dependent mean free path of the photoexcited electrons generated by scattering into the spin polarized holes of the 3d shell.

Spin polarized electron spectroscopy became a major topic in the field of surface and two dimensional magnetism. For the interpretation of any spectra it is indispensable to know how the measured spin polarization - which is defined as $P=(N\uparrow-N\downarrow)/(N\uparrow+N\downarrow)$, where $N\uparrow(\downarrow)$ is the number of emitted electrons with spin parallel (antiparallel) to the magnetization of the sample - is linked to the ground state polarization. In this paper we provide evidence that spin dependent inelastic scattering is the dominant mechanism affecting the polarization of low energy photoelectrons. This is in accordance to recent theoretical and to different experimental work [1-3].

We evaporated Cobalt films, which form an epitaxial fcc (100) structure, with different thicknesses on a sputtered and annealed Cu(100) surface [4]. With Auger electron spectroscopy no contamination was found and LEED showed perfect crystallinity of the Co films. The thickness of the Co film was determined by AUGER spectroscopy. Afterwards the sample was slightly cesiated to lower the photothreshold. This does not affect the polarization, as has been demonstrated in another experiment by our group [2]. For all films the photothreshold, determined by a Fowler plot was 1.55 ± 0.07 eV. A magnetic field of 1.9 Tesla was applied perpendicular to the sample surface to achieve saturation of the films. Monochromatic light of 1.4 to 3.5 eV excited photoelectrons and their spin polarization has been measured in a 100 kV Mott-detector.

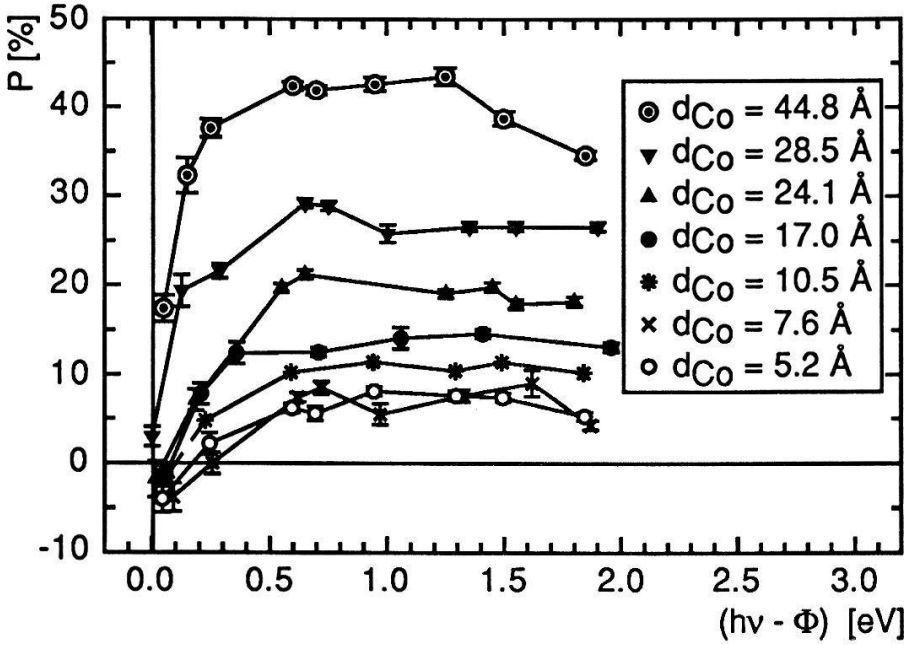

Figure 1: Polarization measurement of the total photoyield of Co/Cu(100) for different Co film thicknesses.

For thick fcc Co films the polarization spectra, shown in Figure 1 are in accordance to the spectra for

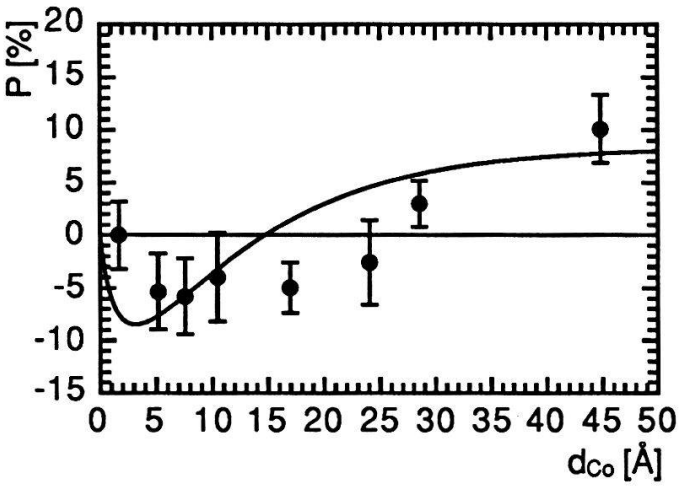

Figure 2: Measured and calculated polarization of the photoelectrons emitted at photothreshold from a d_{Co} thick cobalt film on Cu(100).

bulk hcp Co [2], i.e., the spin polarization is positive at the photothreshold and not negative as would be supposed because of the completely filled majority d-band in ferromagnetic Cobalt [5]. This proves that the polarization is not conserved. A possible explanation of this effect is given by the model developed by Schönhense and Siegmann [6]. It predicts a spin dependent inelastic mean free path generated by the scattering of photoelectrons into the spin polarized 3d holes. Because the 3d-holes are within a few eV above E_F, this spin filter effect should decrease, if one uses light with an energy larger than 10 eV. This has been experimentally confirmed and a negative polarization has been found [7]. According to this theory one would expect that the spin filtering effect also decreases, if the thickness of the cobalt films is in the order of the inelastic mean free path, i.e., the sign of the measured polarization should become equal to the sign of the ground state polarization, which is negative.

To test this hypothesis we evaporated several thin Co films on our Cu(100) substrate and indeed a negative spin polarization of the total photoyield near the photothreshold has been measured (see Figure 1). This means that in a thin film the polarization of the photoelectrons is less altered, which is in accordance to the above model. Due to vanishing small electron counting rates caused by the small light intensities of the monochromatic Hg-Xe lamp between the major emission lines it was not always possible to measure directly at the photothreshold. Nevertheless every measurement has been done closer than 0.05 eV to the threshold. In order to be able to compare the polarization data we extrapolated the polarization spectra as a function of light energy to the photothreshold. This extrapolated polarization at the threshold in function of the film thickness is shown in Figure 2. A clear change in sign at about 27 Å is observed. Above this thickness the number of minority electrons, which are more attenuated than the majority ones, becomes greater than the number of majority electrons and the polarization becomes positive.

We also calculated the thickness dependence of the polarization of Co/Cu(100) at the photothreshold with the above mentioned spin filter model. The calculated curve is shown in Figure 2. The theoretical calculation also shows a change of sign in the polarization, as has been expected. The discrepancy of the zero crossing of the polarization is probably due to the uncertainty in the Auger thickness calibration. It is also possible, that the inelastic mean free paths are larger at our small energies than the values taken out of Reference 6, where the inelastic mean free paths have been measured around 7 eV.

It has been experimentally verified that the polarization of thin Co films is negative as predicted by the model of the spin dependent inelastic mean free path. Furthermore the change in sign of the polarization with increasing thickness is nicely reproduced.

References:
[1] H.C.Siegmann, Surf.Sci. **307-309**, 1076 (1994) and references therein
[2] J.C.Gröbli, A.Kündig, F.Meier, H.C.Siegmann, Physica B **204** 359 (1995)
[3] J.C.Gröbli, D.Guarisco, S.Frank, F.Meier, Phys.Rev. B **51**, 2945 (1995)
[4] M.T.Kief, W.F.Egelhoff, Phys.Rev. B **47**, 10785 (1993)
[5] C.Li, A.J.Freeman, C.L.Fu, J.Magn.Magn.Mater **94**, 134 (1991)
[6] G.Schönhense, H.C.Siegmann, Ann.Physik **2**, 165 (1993)
[7] C.M.Schneider, P.Schuster, M.S.Hammond, J.Kirschner, Europhys.Lett. **16**, 689 (1991)

Helv Phys Acta
Vol. 68 (1995)

0018-0238/95/020203-02$1.50+0.20/0
(c) Birkhäuser Verlag, Basel

SPACE CHARGE FORMATION AROUND A HIGH VOLTAGE CORONA ELECTRODE IN ELECTROSTATIC PRECIPITATORS

W. EGLI and U. KOGELSCHATZ
ABB Coroporate Research , CH-5405 Baden

Abstract: A geometry bounded by two plane grounded plates with parallel wires in the center plane is considered. Different choices of boundary conditions for the current flow respectively the space charge density in the active plasma region at the high voltage electrode result in a drastically different space charge patterns close to the corona electrode. Results are given for three different model assumptions. The influence of adjacent wires leads to well defined structures of the space charge in the vicinity of a corona electrode.

Introduction: The space charge and the electric field distributions together with the flow properties, see e. g. [1], are main parameters influencing the performance of electrostatic precipitators (ESPs). In these particle filters a corona discharge is initiated by applying a negative high voltage to thin corona electrodes that are positioned in the middle plane between two parallel collection plates at ground potential. A particle laden gas flow passing this duct, for example a flue gas stream containing fly ash, can be efficiently cleaned when ions from the corona zone are used to charge the particles and the electrical fields are optimized in such a way that the electrical forces acting on the charged particles drive them to the collection plates. The distance of the plates is of O(10cm), the diameter of the corona electrodes of O(1mm). Fig. 1 shows the electrode configuration of a typical ESP geometry.

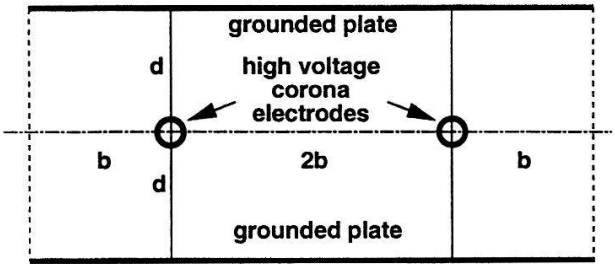

Fig. 1: Cross section of the considered electrode configuration.

Model Assumtions: The active plasma zone (the corona layer) at the high voltage wires is very thin, in air at atmospheric pressure presumably O(10 μm). In this zone the charges are generated: electrons as well as positive and negative ions. The positive ions travel only a short distance to the negative high voltage electrode and free electrons in air attach rapidly to molecules to form negative ions. For simplicity we assume that only one species of negative ions with constant mobility μ leaves this active plasma zone in the direction of the collection plates. Thus, most of the available space is occupied by this passive ion drift region [2].

The equations governing the charge density ρ and the electric field $\mathbf{E}$ in this region are $\mathbf{E} = -\text{grad}\,\Phi$ with $\Delta\Phi = -\rho/\varepsilon$, the equations for the current density $\mathbf{j}$ are $\mathbf{j} = \rho\mu\mathbf{E}$, div $\mathbf{j} = 0$, (Φ: potential, ε: permittivity). The boundary conditions are well defined only at the electrodes: $\Phi = 0$ at the collection plates and $\Phi = U$ at the (negative) high voltage electrodes. Additional assumptions are needed to characterize the charge generation in the active plasma region and the boundary condition at the interface between the plasma and the ion drift region. Since the current must pass through both zones its boundary condition at the interface must in principle contain the lacking information about the active plasma zone. Due to the complexity of the problem this can be done only in an approximate way. To demonstrate the strong influence of the chosen boundary conditions on the result we present three model cases for illustration. In all cases the 4 equations for the physical processes in the ion drift region are solved [3]. The differences in the results are due to the different assumptions about boundary conditions.

Model 1: j_0 = constant at the wire surface. From a specific U-I measurement and the assumption of an uniform corona current density at the wire surface the constant can be evaluated.

Model 2: A more directed current emission towards the collection plate can be simulated by a cosine distribution at the wire, for example: $j_0(\beta) = A\cos^3\beta$. The angle β is measured from the wire surface to the normal of the wire to the plate. This simulation was made in analogy to measured current distributions at the plane of a point plane corona discharge. According to Warburg [4] this current distribution follows a cosine law with an exponent between 4 and 5.

Model 3: In order to incorporate at least the most fundamental gas properties we also used the following model: $j_0 = \rho\mu E$, where $\rho = c\,\bar{\alpha}(E/n)$. This is a first order approximation of the generated charges in the active plasma zone, where $\bar{\alpha} = \alpha - \eta$ is the effective ionization coefficient with α, η representing the ionization and attachment coefficients. A simple analytical approximation for $\bar{\alpha}$ in air at ambient conditions is $\bar{\alpha}\,[m^{-1}] = 68\,(E-E_{crit})^{3/2}$, with $E_{crit} = 23.8$kV/cm [5]. The constant c in this model contains all unknown quantities about the active plasma zone and can be determined from a measured current voltage curve. In this model the active plasma region is characterized by one quantity depending only on E/n. Its outer boundary is given by the condition $\bar{\alpha} = 0$ or $E = E_{crit}$ and is automatically calculated in a way that is consistent with the given geometry and the used equations.

Numerical Results: We compare the three cases for identical applied voltage of 40 kV and an assumed duct width of 2d = 30cm. In Fig. 2 lines of constant charge density are plotted for a relatively small electrode separartion 2b = 22cm and a much wider electrode spacing of 2b = 66cm. The constant c in model 3 was taken as c = 30 nAs/m^2. The free parameters in the other models were chosen to give the same average current densities at the collection plates: 74 μA/m^2 for the narrow spacing and 49 μA/m^2 for the wide spacing.

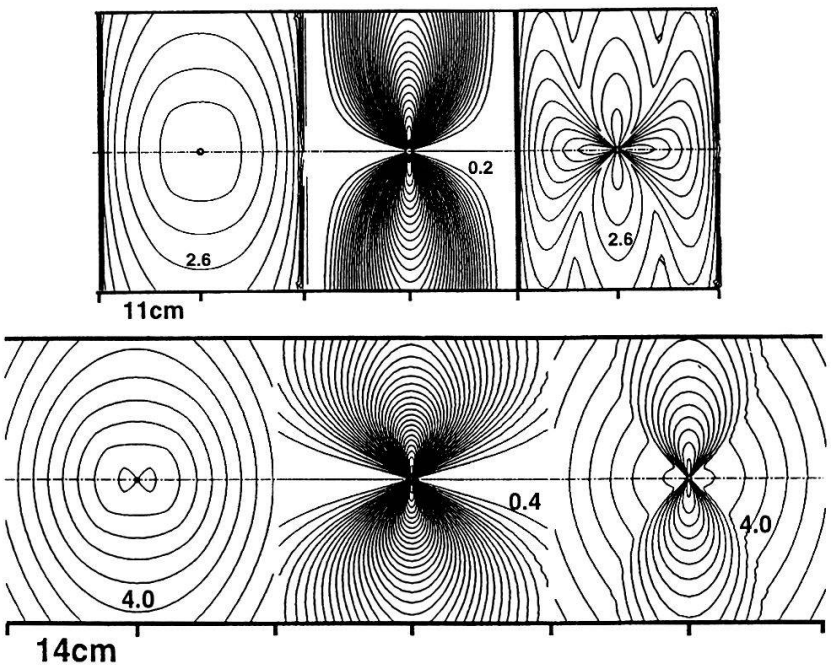

Fig. 2: Space charge density around a cylindrical wire in the wire/duct geometry of Fig. 1. Upper row: narrow electrode spacing, lower row: wider spacing. Model 1 (left), model 2 (middle), model 3 (right). Maximum charge densities in the upper row are: 3.1, 7.3 and 4.0 μAs/m^3 and: 6.1, 13.9 and 8.2 μAs/m^3 in the lower row. Spacing of isolines is 0.2 μAs/m^3 in the upper row and 0.4 μAs/m^3 in the lower row.

Conclusions: It is evident that the different assumptions about the boundary condition at the high voltage electrode have a pronounced influence on the space charge distribution in the ion drift region and that adjacent electrodes show a strong coupling at close spacing. We assume that the third model is the most realistic one because it imposes no artificial restrictions on the spatial extension of the active plasma region. A precise measurement of the local current distribution at the collection plates could be used to check the validity of this assumption.

References

[1] E. Gerteisen, W. Egli and B. Eliasson, Helv. Phys. Acta **67** (1994), 769 - 770

[2] R.S. Sigmond and M. Goldman in *Electric Breakdown and Discharges in Gases*, E.E. Kunhardt and L.H. Luessen (eds.), NATO ASI Series, Plenum 1983, p.1 - 64

[3] W. Egli, O. Riccius, U. Kogelschatz, R. Gruber and S. Merazzi, 6. Joint EPS-APS International Conference on Physics Computing: PC '94, Lugano 1994, 535 - 541

[4] E. Warburg, Wied. Ann. **67** (1899), 69

[5] R.T. Waters and W.B. Stark, J.Phys. D: Appl.Phys. **8** (1975), 416 - 426

Helv Phys Acta
Vol. 68 (1995)

0018-0238/95/020205-02$1.50+0.20/0
(c) Birkhäuser Verlag, Basel

Influence of visible light on flux creep in HTS films

I. L. Landau and L. Rinderer

Institut de Physique Expérimentale, Université de Lausanne, 1015 Lausanne-Dorigny

We present an experimental study of the flux creep rate in YBCO film at low temperatures. It is shown that the flux creep can be described in terms of quantum tunneling of vortices up to temperatures of 10-15 K. We have investigated also the influence of a weak illumination on a flux creep rate. It is shown that a visible light with intensity as weak as 1 mW/cm^2 drastically changes the flax creep rate at liquid helium temperatures. We propose a simple model to explain this extreme sensitivity of the flux creep to a weak illumination.

A very high sensitivity of the flux creep in HTS to a visible light has been discovered by Yurgens and Zavaritskii on Bi-2212 single crystals [1]. Here we present experimental investigation of this effect made on YBCO film. We used a ring shaped film and it gave us a possibility to obtain directly voltage-current (V-I) characteristics of the sample in a flux creep regime.

The measurements were made on a ring made of 0.3 mkm thickness YBCO film. The external diameter of the ring was 10 mm and the width was 1 mm. A transverse magnetic field of 0.16 T was used to form a vortex structure and to induce a current in the ring. After the switching off the external field the magnetic field inside the ring was monitored as a function of time. This magnetic field is connected with the current through the ring. A voltage around the ring is proportional to a time derivative of the magnetic flux inside the ring. Thus, both quantities can be calculated.

Typical V-I curves of the ring are shown in Fig. 1. One can see that the main influence of the temperature rise is a practically parallel shift of V-I curves along j-axis. The influence of the illumination is completely different and the main effect here is a change of the slope.

At low temperatures the main mechanism of the flux creep is a quantum tunneling of vortices [2]. Electric field in this case can be written as

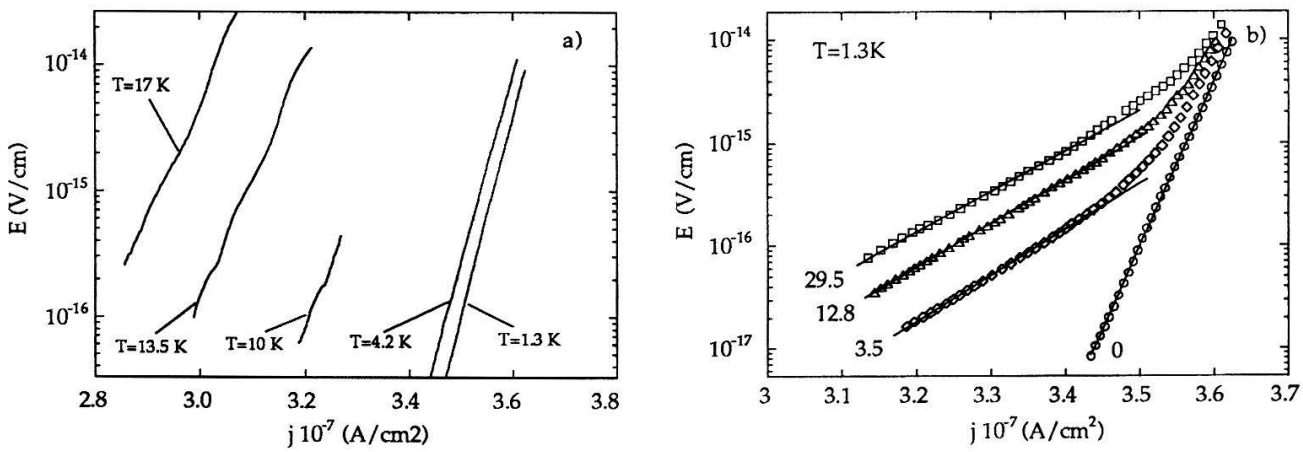

Fig. 1. Electric field versus current density. a) At different temperatures without illumination. b) For different light intensities. Numbers near the curves show a light power in mW/cm^2.

$$\log E = \log E_0 - \frac{S}{\hbar} + \frac{S}{\hbar}\frac{j}{j_c}$$

where S is the Euclidean action of the tunneling process, j_c is the critical current, and E_0 is a constant connected with the attempt frequency, magnetic induction, etc. It should be noted that the temperature dependence of the flux creep rate without illumination is in very good agreement with theoretical calculations for the quantum creep [2] in the temperature range 1.3 - 15 K with the quantum crossover temperature of about 20 K.

There exists no theory to consider the influence of light on the flux creep and here we can propose only a simple qualitative model. The photon energy ε is much higher than the superconducting energy gap Δ and the main channel of the light absorption is a breaking of Cooper pairs. The difference $(\varepsilon - \Delta)$ turns into kinetic energy of two normal excitations formed in this process. These excitations loose their energy due to different inelastic processes. It can be an interaction with phonons and other normal excitations as well as breaking of other pairs. After loosing of their excessive energy the excitations can recombine with a formation of a new Cooper pair. This process accompanies by irradiation of a phonon with an energy equal to Δ. The important point is that the energy gap in HTS is few hundred Kelvin and it is very difficult to irradiate such a phonon at low temperatures. Usually the probability of the phonon irradiation is proportional to their number. However, there are practically no such phonons at low temperatures and the relaxation must be very slow. We believe that it is the only reasonable explanation of the effect.

Eq. (1) shows that Euclidean action S can be defined from slopes of V-I curves as well as from values of logE(j=0). The normalized values of S plotted in Fig. 2 as a function of the light power (open and filled symbols correspond to two different ways of calculation of S). One can see that a straight line is a very good approximation for the data. Extrapolation of this straight line shows that even an illumination as weak as 10^{-9} W/cm^2 should have a noticeable influence on the flux creep. However, it can be observed only for very low electric fields (see Fig. 1b); this situation corresponds to very long times after switching off the magnetic field in our experimental arrangement.

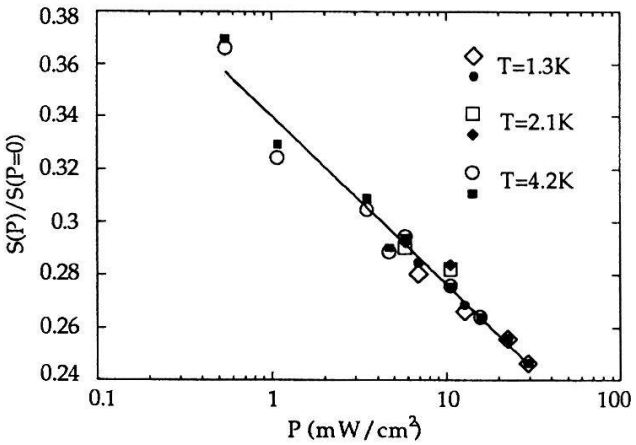

Fig. 2. Normalized Euclidean action versus the light power. S(P=0) is the value of S at T=4.2K and P=0.

References

1. A.A. Yurgens and N.V. Zavaritskii, Physica C **203**, 277 (1992)
2. G. Blatter and V. Geshkenbein, Phys. Rev. B **47**, 2725 (1993)

Helv Phys Acta
Vol. 68 (1995)

0018-0238/95/020207-02$1.50+0.20/0
(c) Birkhäuser Verlag, Basel

THE KOSMA 3-M SUBMILLIMETER WAVE TELESCOPE ON GORNERGRAT

C.G. DEGIACOMI and J. STUTZKI
I. Physikalisches Institut, Universität zu Köln, D-50937 Köln, Germany

Abstract.
The 3 m KOSMA telescope at Gornergrat is dedicated to millimeter and submillimeter wave astrophysics with observations mainly of interstellar atomic and molecular lines. This includes measurement of the large scale structure and dynamics of molecular clouds in our galaxy for a better understanding of the processes connected with star formation. The present research activity of the observatory is presented with a special scope on the description of the techniques and instrumentation used. A new 3 m reflector for the KOSMA telescope with an expected surface accuracy of 10 μm is under construction. With this new instrument and the excellent quality of the atmosphere at the site operation into the THz region (λ=200 μm) will be possible.

1. Introduction

The "Kölner Observatorium für Sub-Millimeter Astronomie" (KOSMA) is in operation since 1986 on Gornergrat near Zermatt. It's 3 m antenna was designed for observations in the millimeter and submillimeter spectral range covering the transparent atmospheric window below 450 GHz. The observation of interstellar molecular lines using their characteristic rotational transition frequencies allowed the identification of more than 100 detected molecules up to date.

The excellent atmospheric conditions on Gornergrat with the precipitable water vapor being often below 1 mm in winter time allows observations in the highest frequency atmospheric windows at 660 GHz and 880 GHz. Similarly dry conditions are found only at very few sites, e.g. on Mauna Kea (Hawaii). In order to observe at these high frequencies the KOSMA telescope reflector gets replaced by one with a higher surface accuracy. The now mature techniques allows to fabricate a radiotelescope with a sufficient surface precision.

2. Observations with the KOSMA Telescope

The main scientific emphasis of the research at KOSMA are primarily measurements of large scale distributions, structure and dynamics of molecular clouds as well as the dedicated search for new molecular species. The relatively low abundance of heavy atom compounds, e.g. carbon monoxide, can be used as a diagnostic tool for the physical and chemical state of the bulk of the interstellar gas. Beside this, a few atomic fine structure line are accessible to observations from the ground. The molecular component of the interstellar gas builds giant clouds. These clouds are highly turbulent and show a very complex filamentary and clumpy structure on all scales. The smallest fragments have about solar mass size which may eventually collapse into new stars. The details of this star formation process are the target of active research and are at present far from being resolved.

A small telescope with its correspondingly moderate angular resolution is ideally suited for the study of the large scale structure and dynamics of molecular clouds. A very fruitful application for a small telescope is the combination of observations of different size telescopes thus covering a much larger range in spatial frequencies. Even for high angular resolution observations with a large telescope, complementary observations with a small telescope can be essential, e.g. by allowing to correct for the errors introduced by the error beam of the large telescope.

3. The new KOSMA Telescope

In order to get a better understanding of the processes connected with star formation, two major scientific trends have emerged: first, the drive to higher frequencies in order to observe new molecular species and probe different temperature and density regimes; second, the quest for higher spatial resolution for revealing the dynamical, physical, and chemical processes of star formation and its evolution. The latter is the field of radio interferometers.

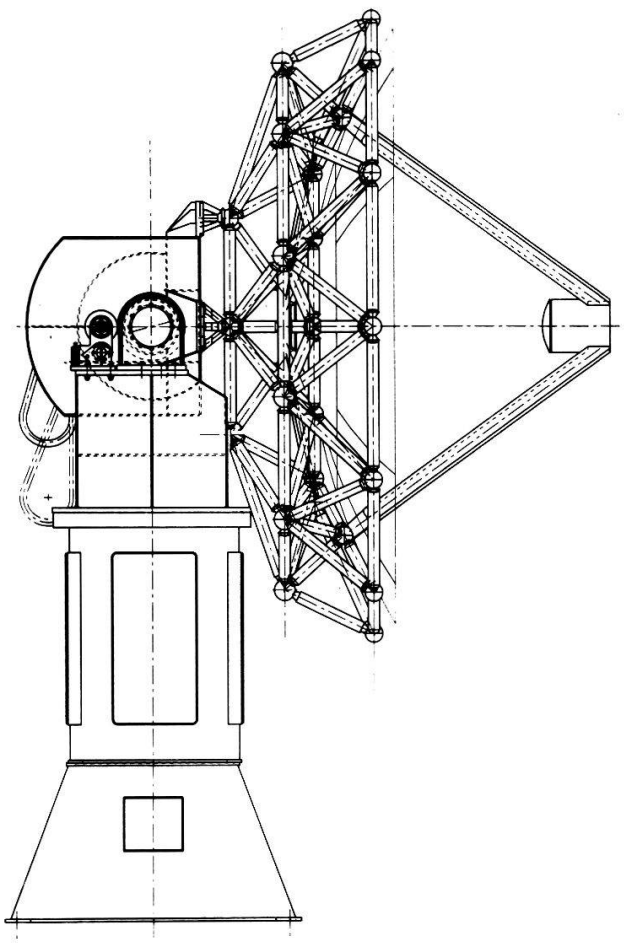

Fig. 1. Schematic of the new KOSMA 3-m telescope.

TABLE I
Characteristics of the new KOSMA telescope.

Main reflector	
Shape	parabolic
Diameter	3 m
f-ratio	0.43
Surface	10 μm r.m.s.
Construction	18 aluminum panels
Coating	SiO_2 for protection
Backstructure	CFRP framework
Alignment	actuator on each panel corner
Subreflector	
Shape	hyperbolic
Diameter	270 mm
Surface	4 μm r.m.s.
Construction	aluminum with SiO_2 coating
Alignment	5 degrees of freedom
Chopper	cross-elevation, $\pm$3' on sky, 4 Hz
Telescope	
Type	Cassegrain
f-ratio	10.4
Focal length	31200 mm
Mount	altitude-azimuth
Observing Ports	2 on each side of the elevation axis
Loads	hot and cold load for calibration

In order to take advantage of the good atmospheric conditions on Gornergrat for future highest frequency observations a new telescope with a better surface accuracy is under construction. Table I lists the design parameters of this new telescope. A detailed description of this new KOSMA telescope can be found in Degiacomi et al. (1995). The final contour of the 18 aluminum reflector panels will be made on a diamond mill. The complete telescope will have a surface accuracy of 10 μm rms under all load conditions such as thermal expansion and gravity. With the new telescope design (Fig. 1) it will be possible to have two receivers mounted simultaneously at the telescope in a Nasmyth arrangement along the elevation axis. This allows an optimum operation of receivers at different frequencies depending on the atmospheric conditions. A secondary mirror chopper allows beam switching in cross-elevation up to a frequency of 4 Hz.

4. Conclusion

Observations in the highest atmospheric windows around 660 GHz and 880 GHz will be performed with the new KOSMA telescope presently under construction. With this telescope and the very sensitive SIS receivers elements as well as the acousto-optical spectrometers new results in the mm- and submm-wave spectral range will be revealed soon from the Gornergrat.

References

Degiacomi, C.G., Schieder, R., Stutzki, J., Winnewisser, G.: 1995, 'The KOSMA 3-m Submillimeter Wave Telescope on Gornergrat: Interstellar Spectroscopy and Astrophysics', *Optical Engineering* , in press

Helv Phys Acta
Vol. 68 (1995)

0018-0238/95/020209-02$1.50+0.20/0
(c) Birkhäuser Verlag, Basel

The influence of boundary conditions to bluff body wakes in fully developed pipe flow

F. Ohle

Institut für Angewandte Mechanik und Strömungsphysik der Universität,
D-37073 Göttingen Bunsenstr. 10, FRG

Boundary conditions of fluid-mechanical systems have a strong impact in the observed dynamical behavior. In this work the wake behind a circular cylinder in fully developed pipe flow is investigated. It will be shown that the aspect ratio of the cylinder have a strong impact on the frequency laws. The observed deviation of the frequency laws for different aspect ratios, and the occurrence of frequency discontinuities and frequency cells in the wake flow are discussed. Furthermore the positive effect of using a turbulence grid mounted in front of the circular cylinder is shown.

More than one hundred years after the discovery of the aeolian tones by Strouhal [1], vortex streets behind bluff bodies have been a very active field of research. The properties of such flows depend in general on the Reynolds number $Re = Ud/\nu$, where U is the velocity of the oncoming flow, d is the cylinder diameter, and ν is the kinematic viscosity of the fluid. Recently it was shown, that the aspect ratio of the cylinder, i.e. the length-over-diameter ratio (l/d) and the end conditions of the bodies have a strong impact on the characteristic features of the wake flows. The influence of such parameters for $50 \leq Re \leq 300$ has been confirmed experimentally in laminar channel flow by a variety of works (for an overview see Ref. [2]). Here different Sr-Re relationships were found for various l/d and end-conditions, where the Strouhal number is defined by $Sr = fd/U$ (f : shedding frequency).

In the following it will be discussed how the l/d-ratio or the end-conditions play a role in the wake behind bluff bodies mounted in fully developed pipe flow. In general most technical pipe flows are turbulent and the profile of the flow field is not homogeneous compared the work introduced above. This fact as well as small aspect ratios used in real applications, i.e. $4 \leq l/d \leq 6$, have a strong impact on the global wake structure. The measurements presented here have been carried out in a circular pipe with a length of $10.5m$ and a diameter of D=$0.05m$. A circular cylinders with a diameter of d=0.3, 0.6, 1.0 or $1.37cm$ is placed horizontally in the middle of the test section at the end of the pipe. A hot-wire probe was mounted in the wake of the cylinder to measure the velocity fluctuation. In some parts of the investigations a mesh structure, which is called turbulence grid in the following, was mounted $15cm$ in front of the cylinder to disturb the pipe flow.

In Fig. 1 the Sr-Re relationship for different cylinder diameters of d=3, 6, 10 and $13.7mm$ is shown. Due to the d/D-ratio for the cylinder of d=$10mm$ and $13.7mm$ the effect of the compressibility of the fluid can be obtained by a strong deviation of the Sr-Re relationship to the classical development represented by the cylinder of d =$3mm$ and $6mm$. Therefore, it is not possible to derive a unique Sr-Re relationship for such flow-configurations. Next the influence of a turbulence grid with a wire distance a_w and a wire thickness d_w mounted in front of the cylinder is discussed. In Fig. 2 the Sr-Re-relationship for a circular d=$10mm$ with an undisturbed pipe flow and pipe flows which is influenced by a turbulence grid of a_w=$4mm$

and d_w=1mm, and a_w=3mm and d_w=0.7mm is plotted. Here it is found, that only small variations of Sr compared to the undisturbed pipe flow occur. The positive effect is obtained by the signal-to-noise ratio, where the quality of the experimental data is improved by about 15 dB compared to the undisturbed flow. Furthermore, it is possible to measure accurately the shedding frequencies at lower velocities. This is due to the fact, that the grid forces an earlier transition from a laminar to a turbulent flow, in which a better quality of the measured data is obtained. If no passive or active control mechanism are used different frequency cells in the wake of the cylinder can occur. In Fig. 3 the frequency cells for a centerline velocity of $U_{cl} = 7m/s$ along the z-axis of a cylinder of d=3mm and 6mm are presented. In technical applications such cell structures are undesirable, since the cells structures are not stable and therefore deviations to the calibrated frequencies can occur. In this work it was found that such cells can be suppressed by the use of the turbulence grids. The effect is illustrate in Fig. 4, where the frequency distribution of a cylinder of d=3mm for two different velocities are shown. The obtained result might be due to the fact, that the turbulence level of the fluid is increased and more uniformed and therefore reduces irregularities of the velocity profile. Since all possible velocity vectors (u, v, w) now have a non-neglecting values, disturbances are exponentially increased and may causes the loss of lock-in regions of the cells [2].

References

[1] V. Strouhal, Ann. Phys. und Chemie, Neue Floge **5**, 216 (1878)
[2] M. König, H. Eisenlohr and H. Eckelmann, Phys. Fluids A **2**, 1460, (1990)

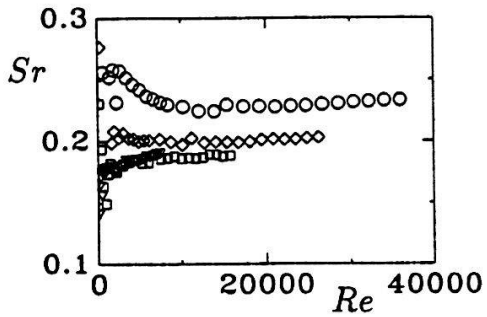

Fig. 1: Strouhal numer versus the Reynolds number for circular cylinders with different cylinder diameters. ∇ : $d = 3mm$, $\square$: $d = 6mm$, $\diamond$: $d = 10mm$, and $\circ$: $d = 13.7mm$.

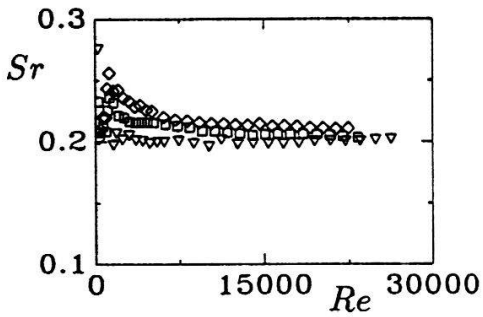

Fig. 2: Strouhal numer versus the Reynolds number for a circular cylinder of $d = 10mm$ in undisturbed pipe flow (∇) and pipe flows which is influenced by a turbulence grid of $a = 4mm$ and $d_w = 1mm$ ($\square$), or $a = 3mm$ and $d_w = 0.7mm$ ($\diamond$), respectively.

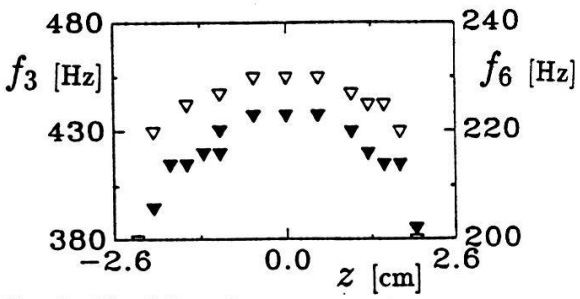

Fig. 3: Shedding frequencies behind the a cylinder versus the location z of the probe in spanwise direction. $\blacktriangledown$: $d = 3mm$ ($f_3[Hz]$), and ∇ : $d = 6mm$ ($f_6[Hz]$). $U_{cl} = 7.1\frac{m}{s}$

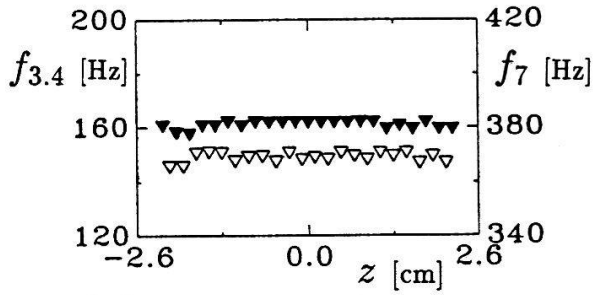

Fig. 4: Cell structure behind a cylinder of $d = 3mm$ for differen velocities. $\blacktriangledown$: $U_{cl} = 3.4\frac{m}{s}$ ($f_{3.4}[Hz]$) and ∇: $U_{cl} = 7\frac{m}{s}$ ($f_7[Hz]$) where a turbulence grid with $a = 4mm$ and $d_w = 1mm$ was used

Helv Phys Acta
Vol. 68 (1995)

0018-0238/95/020211-02$1.50+0.20/0
(c) Birkhäuser Verlag, Basel

Low-dimensional modeling of the separation of bluff body wakes

F. Ohle and M. Lange

Institut für Angewandte Mechanik und Strömungsphysik der Universität,
37073 Göttingen, Bunsenstr. 10, FRG

In this work we propose a novel method to measure the dynamics of the cylinder wake via the pressure fluctuations in the boundary layer of the cylinder produced by the separating wake. It will be shown that this new experimental arrangement can measure the characteristic features of the wake flow or the pressure fluctuations from which a low-dimensional model for the dynamics of the separated wake can be derived. The outcoming results are in very good agreement with similar investigations using classical measurement technics such as the hot-wire anemometry.

A challenging question in fluid mechanics is still the active control of wake flows behind bluff bodies [1]. Up to now, there has been no break through of this problem, because such wakes are more or less nonlinear and therefore traditional linear control methods might not fit. In this paper results are presented which relies on the idea of a nonlinear model-based control. The concept of such a control, is based on having an accurate model of the unperturbed system from which an appropriate driving force can be calculated [2].
In this work the wake behind a circular cylinder in the periodic regime ($50 \leq Re = U_\infty d/\nu \leq 160$; U_∞: flow speed, d: cylinder diameter, ν: kinematic viscosity) is considered. It has been shown elsewhere [2-4], that for such cylinder wakes a LDM can be extracted from measured time signals. From these LDM's the response to external sound excitation can be predicted. In general the external sound excitation is a simple but effective experimental method to stimulate or stabilize the wake flow behind bluff bodies [1,3,4]. Unfortunately, this type of stimulation possesses some physical problems for the control, since in some cases the exact transfer of the calculated control functions is not possible. Therefore, taking the physical properties of the wake into account the new experimental setup proposed in this work is of the following type (Fig. 1): The center-piece of the new arrangement is a cylindrical pipe which replaces the natural cylinder. In the later experiment the separation of the vortices, i.e. the pressure fluctuation $p(t)$ in the boundary layer of the cylinder should be measurement and controled. This can be done using a distribution of equidistant pinholes in one plain of the vertical axis at the cylindrical pipe. The ends of the cylindrical pipe are equiped with endplates and end cylinders to suppress the three-dimensional vortex pattern [3]. In addition, on the one side of the pipe a pinhole-microphone is placed to measure the pressure fluctuation inside, and on the other side a control apparatus can be mounted to suck or blow air out of the pinholes. In this work the control-end was closed.
One of the important feature of this arrangement is the modeling of the dynamics of the separation process. Similar to the ansatz of the model reconstructed for the velocity fluctuations $u(t)$ which are measured in the wake downstream [2-4], a model of the type

$$\ddot{p} = \frac{d^2p}{dt^2} = \sum_{\substack{i=0,\ldots,3 \\ j=0,\ldots,3-i}} b_{ij} p^i \dot{p}^j \tag{1}$$

has been chosen. The coefficients b_{ij} of the model reconstructed from the pressure fluctuations of a separated wake at $Re = 100$ and the corresponding coefficients a_{ij} of the model for the

velocity fluctuations are shown in table 1. It can be seen, that some of the coefficients have similar values. Furthermore it is found by a numerical integration, that the normalized limit cycle of the trajectory of the velocity and the pressure fluctuations are in a good agreement.
A very useful tool for the analysis of the reconstructed coefficients and to estimate the quality of the model was introduced by [4] and is based on the following idea: For slowly varying amplitudes and frequencies, the general oscillator equation (Eq. 1) can be approximated by the Landau equation

$$\dot{r} = \alpha r - \beta r^3, \qquad \dot{\varphi} = -\gamma - \delta r^2,$$

where r is the amplitude and $\omega := \dot{\phi}$ the circular frequency. The corresponding Landau coefficients can be calculated from

$$\alpha = \frac{1}{2}a_{01}, \quad \beta = -\frac{1}{8}(a_{21} + 3a_{03}), \quad \gamma = \frac{1}{2}(1 - a_{10}), \quad \delta = -\frac{1}{8}(a_{12} + 3a_{30})$$

The resulting Landau coefficients of table 1 are shown in table 2. The coefficient α is a measure for the instability of the fixpoint $r = 0$ and $\beta > 0$ defines the damping of the oscillator at large amplitudes. Since we have normalized the data [4], the circular frequency $w_g = 1$ and the amplitude of the limit cycle $r_g = 1$, where $r_g = (\alpha/\beta^{1/2}$, and therefore $\alpha = \beta$. The value of γ represents the circular frequency for small amplitudes, wheres δ describes the increase of the frequency for a corresponding increase of the amplitude. For the reconstructed coefficients for the pressure fluctuations (table 2) β shows a larger value compared to the velocity fluctuations. This indicates a faster transient to the asymmpotic solution, whereas the deviation of the amplitude-frequency coupling (δ) for the pressure and the velocity, which is an essential physical property for the no-feedback control or a nonlinear resonant stimulation is very small [1]. These results indicate, that it is possible to measure the pressure fluctuation via the new experimental arrangement and therefore, a very effective application of the nonlinear no-feedback method can be expected.

References

[1] F. Ohle and M. Lange, submitted to Phys. Rev. E (1995)
[2] A. Hübler and E. Lüscher, Naturwissenschaften **76**, (1989)
[3] F. Ohle and H. Eckelmann, Phys. Fluids A **4**, 1702, (1992)
[4] F. Ohle, MPI für Strömungsforschung, Report Nr. 17/1992, (1992)

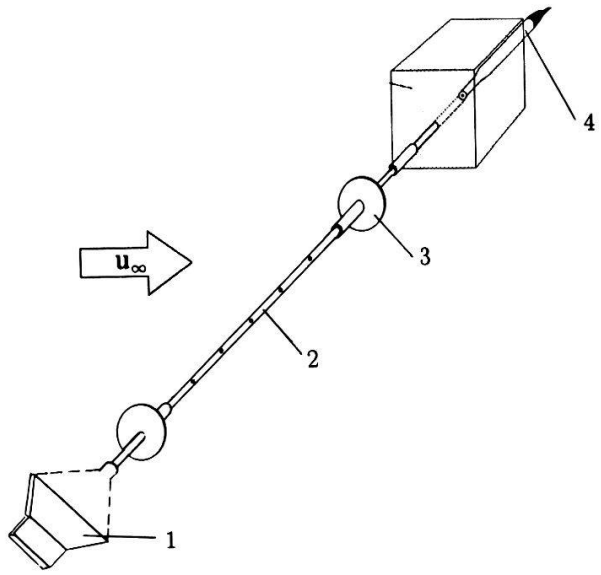

Fig. 1: Schematic presentation of the modified experimental set-up. 1: control apparatus, 2: cylindrical pipe with n pin-holes, 3: endplates with endcylinders and 4: pin-hole microphone.

i	j	$a_{ij}(u)$	$b_{ij}(p)$	i	j	$a_{ij}(u)$	$b_{ij}(p)$
0	0	0.000	0.000	1	1	0.420	0.518
0	1	0.149	0.260	1	2	0.026	0.026
0	2	-0.030	0.144	2	0	-0.144	-0.142
0	3	-0.137	-0.232	2	1	-0.187	-0.343
1	0	-1.000	-1.000	3	0	-0.069	-0.072

Table 1: Comparison of the reconstructed coefficients of the velocity ($a_{ij}(u)$) and pressure fluctuations ($b_{ij}(p)$) for a vortex street at $Re = 100$.

	$u(t)$	$p(t)$		$u(t)$	$p(t)$
α	0.0747	0.12975	γ	1.0000	1.0000
β	0.0747	0.12975	δ	0.0226	0.0237

Table 2: Landau coefficients od Eq. 1 for the coefficients of table 1.

Helv Phys Acta
Vol. 68 (1995)

0018-0238/95/020213-02$1.50+0.20/0
(c) Birkhäuser Verlag, Basel

Three-dimensional phenomena in bluff body wakes

F. Ohle and Chr. Steinhoff

Institut für Angewandte Mechanik und Strömungsphysik der Universität,
37073 Göttingen, Bunsenstr. 10, FRG

The Kármán vortex street behind a delta-shaped bluff body in a laminar homogeneous core is experimentally investigated. The main emphasis here is to investigate three-dimensional phenomena of the vortex street in the range of $50 \leq Re \leq 150$. We will show that the end-condition of the bluff bodies have a strong influence on the Strouhal-Reynolds number relationship, i.e. oblique vortex shedding with various shedding angles can occur. The results indicate that three-dimensional vortex shedding phenomena are independent processes of the shape of the body.

The wake of bluff bodies in the low Reynolds number range of $50 \leq Re = U_\infty d/\nu \leq 160$, where U_∞ : mean stream velocity, d : cylinder diameter and ν : kinematic viscosity, is characterized by an array of vortices shedding from the body. A number of recent investigations have been focussed on the three-dimensional aspects of such wake behind circular cylinders [1-4]. Here it was found that the end-condition of finite cylinders have a strong impact on the wake flow and are the main physical parameter to induce parallel or various oblique vortex shedding pattern.

The measurements were carried out in the open-circuit type wind tunnel described in detail by Ref. [3]. To investigate the three-dimensional wake flow phenomena, such as oblique vortex shedding with various shedding angles Θ, a delta-shaped body with a front width of 3.5cm and a depth of 4.4cm was used. In the present study the wake flow phenomena are illustrated by flow visualization using the smoke wire technique [2].

In the following the vortex street behind the above introduced body is investigated for $Re = 100$. In Fig. 1 the flow visualization of parallel vortex shedding is presented, which frequently occur similar to the so-called chevron pattern shown in Fig. 2. In general states both states represent very unstable solution of the wake and can be found for special end-conditions of the body or in the beginning of an experiment [1]. Similar to the above flow structures, for the same Reynolds number presented here, various oblique vortex shedding phenomena with shedding angles Θ in the range of $19^o \leq \Theta \leq 36^o$ are found. In Fig. 3 and 4 the flow visualization of oblique vortex shedding with an angle of $\Theta = 19^o$ and $\Theta = 36^o$ are shown. The occurrence of all possible flow states can be not predicted, and therefore might a stochastical process depending on the turbulence level of the oncoming flow, the surface structure and the quality of the body. Therefore, in the experiments presented here, the Strouhal numbers Sr ($Sr = f \cdot d/U_\infty$, f : dominant frequency) found for two different end-conditions (the body was equiped with and without end-plates) do not collapse with discrete vortex shedding modes found by other authors for circular cylinders [1-3]. For the delta body only one characteristic Sr-Re-relationship was found. A statistical analysis of the occurrence of the obtained flow pattern by the use of an array of hot wire probes in the wake of the body to measure the characteristic frequencies and shedding angles is in progress.

References

[1] C.H.K. Williamson, J. Fluid Mech. **206**, 579, (1989)
[2] M. König, H. Eisenlohr and H. Eckelmann, Phys. Fluids A **2**, 1460, (1990)
[3] B.R. Noack, F. Ohle and H. Eckelmann, J. Fluid Mech. **227**, 293, (1991)
[4] M. König, B.R. Noack and H. Eckelmann, Phys. Fluids A **5**, 1846, (1993)

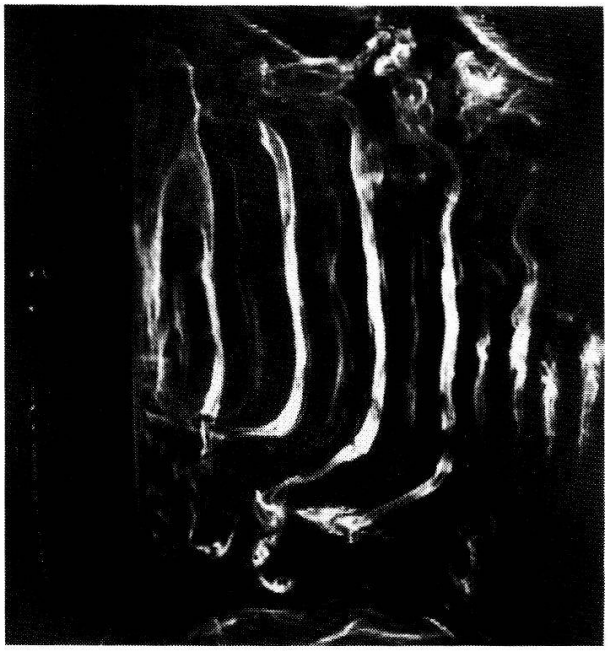

Fig. 1: Flow visualization of the wake behind the delta-shape body (x-z-plane) at Re=100. Here parallel shedding is obtained ($\Theta = 0^o$). The flow is from left to right

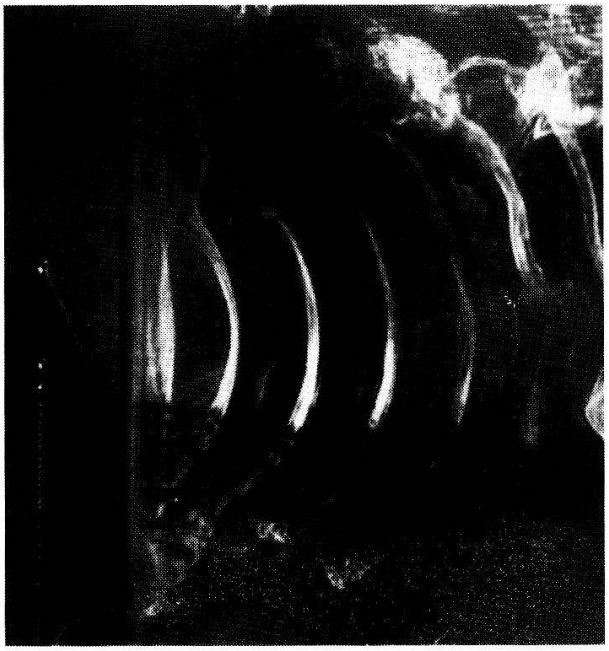

Fig. 2: Same as Fig. 1, but here the so-called cevron pattern [1] temporarily occur in the fully developed channel flow.

Fig. 3: Same as Fig. 1, but here oblique vortex shedding is obtained, with a shedding angle of $\Theta = 19^o$.

Fig. 4: Same as Fig. 3, but here $\Theta = 36^o$.

Helv Phys Acta
Vol. 68 (1995)

0018-0238/95/020215-02$1.50+0.20/0
(c) Birkhäuser Verlag, Basel

A dynamical system approach to flutter instabilities

F. Ohle[+], L. Völkering[*] and G. Schewe[*]

[+] Institut für Angewandte Mechanik und Strömungsphysik der Universität Göttingen
[*] Institut für Aeroelastik, DLR Göttingen, D-37073 Göttingen, Bunsenstr. 10, FRG

Flutter vibrations arise from fluid forces induced by vibration of bluff or streamlined bodies in a fluid flow. In this work a dynamical system approach for the problem of modeling such oscillatory motion is proposed. The emphasis is to reconstruct a model system from measured data of two coupled limit cycle oscillators, namely the oscillatory motion of plunge and torsion. The advantage of this ansatz is that physical parameters like the shape of the cross section, the stiffness or the viscous damping in plunge and torsion do not have to be measured or calculated explicitly. Finally we propose an adaptive nonlinear control mechanism, which suppresses the aerodynamically induced oscillation effectively.

The flutter phenomenon is a self-excited oscillation, caused by the interplay of aerodynamic elastic and inertia forces. It describes a classical bifurcation phenomenon where at a critical flow velocity the steady state of the system becomes unstable against an oscillatory state. Usually the term flutter is applied for at least two-degrees-of-freedom systems, where the structure is an airfoil in attached flow. Classical or binary flutter can occur even at small angle of attack and requires two elastic degrees of freedom the torsion and plunge mode. Galloping of bluff bodies and stall flutter is associated with the occurrence of flow separation and can be obtained even in one-degree-of-freedom systems.

In the following we will focus on the classical binary flutter mechanism. A general model for such flutter problems, which can be expressed by the classical spring supported airfoil, is represented by the equation of motion for a two-degree-of-freedom system with a single bending and a single torsional mode, i.e.

$$\begin{aligned} m\ddot{y} + 2m\eta_y\omega_y\dot{y} + S_x\ddot{\theta} + k_y y &= F_y \\ J_\theta\ddot{\theta} + 2J_\theta\eta_\theta\omega_\theta\dot{\theta} + S_x\ddot{y} + k_\theta\theta &= F_\theta, \end{aligned} \tag{1}$$

where y is the vertical displacement at the elastic axis, θ defines the angle of twist, F_y is the vertical aerodynamic force per unit span at the elastic axis, F_θ is the aerodynamic moment per unit span at the elastic axis, ω_y and ω_θ are the circular frequencies of the oscillators, k_y and k_θ are spring constants and η_y and η_θ are damping factors. The mass per unit length m, the mass moment of inertia J_θ , and the lateral position of the center of gravity S_x are given by $m = \int_A \mu d\xi d\zeta$, $J_\theta = \int_A(\xi^2 + \zeta^2)\mu d\xi d\zeta$, and $S_x = \int_A \xi\mu d\xi d\zeta$, where μ is the density, ξ and ζ are coordinates fixed to the cross section, and A denotes the cross sectional area. The steady lift and moment per unit span on an airfoil are expressed in terms of the lift coefficient C_L and the moment coefficient C_M, i.e. $F_y = \frac{1}{2}\varrho U^2 c C_L$, and $F_\theta = \frac{1}{2}\varrho U^2 c^2 C_M$, where U is the free stream velocity and c is the cord length of the airfoil. The nonlinearity of the system lies in the aerodynamic coefficients, which depend on the angle of attack α, i.e. $C_L(\alpha)$ and $C_M(\alpha)$. Using this type of aerodynamic coefficients, the model for the aerodynamic forces is quasisteady and

restricted to small α, where $\alpha = \theta + \dot{y}/U$ [1] and corresponds to the effective angle of attack of the co-ordinate system of the airfoil. For a given experimental model system, there are a number of free parameters, which have to be measured or calculated explicitly.

The alternative approach to the above introduced aeroelastic problem presented here is based on the idea that both oscillators, i.e. plunge and torsion, of the two-degree-of-freedom system are considered as a coupled dynamical systems. Then the modeling of such systems can be done by the following two steps. First, the measured time signals of plunge $x_p(t)$ and torsion $x_t(t)$ are represented as trajectories in a two-dimensional state space. Second, from this representation a coupled system of two-dimensional ordinary differential equations of the type

$$\begin{aligned} \ddot{x}_p &= \sum_{\substack{i,j,k,l=0,\ldots,3 \\ |i|+|j|+|k|+|l|\leq 3}} a_{ijkl} x_p^i \dot{x}_p^j x_t^k \dot{x}_t^l \\ \ddot{x}_t &= \sum_{\substack{i,j,k,l=0,\ldots,3 \\ |i|+|j|+|k|+|l|\leq 3}} b_{ijkl} x_p^i \dot{x}_p^j x_t^k \dot{x}_t^l \end{aligned} \tag{2}$$

is derived and is used as a model for the description of the temporal dynamics [2]. In Eq. 2 $\dot{x}_i$ and $\ddot{x}_i$ are the first and second time derivatives of the oscillatory motion of the plunge and the torsion, a_{ijkl} and b_{ijkl} are the coefficients of the taylor-series expansion and t is the time. Since Eq. 2 contains the important dynamical behavior of the analysed system, like the stability criteria, the basin of attraction, etc., no further physical parameters compared to the ansatz of Eq. 1 is needed. In general, if the investigated aeroelastic system is subcritical and no flutter instability is obtained, then the coupling of Eq. 2 between plunge and torsion is weak, i.e. the nonzero coupling terms are very small. If the critical velocity is reached, than due to increase of the aeroelastic coupling, the flutter instability is obtained. A great advantage of the proposed ansatz is that although Eq. 2 is not obtained from an analytical ansatz, it can be used for stability analysis, forecasting, to nonlinear resonantly stimulate or to direct a system with no feedback to a preselected dynamics [3].

The suppression of the aerodynamically induced oscillation by effective control mechanism is of great importance in many technical applications. Recently a new approach in the field of controling nonlinear oscillators without feedback has been developed, where the characteristic driving forces have a nonsinusoidal time dependence [3]. This technique which is also known as a model-based control relies on the idea that the dynamics of the unperturbed system can be described by a low dimensional model. In the present case for a chosen airfoil the model system (Eq. 2) is approximately known, and therefore the characteristic features of the coupled oscillators, such as eigen-frequencies and oscillation amplitudes, might only dependent on U_∞. If the coefficients a_{ijkl} and b_{ijkl} of Eq. 2 have a predictable constant time dependence(i.e. $a_{ijkl}(U)$ and $b_{ijkl}(U)$), then it is possible to apply a modified nonlinear adaptive control mechanism [4]. Here in order to backup the model the response of the experimental system $x_i(t)$ is measured from time to time.

References

[1] R.D. Blevins, Flow-Induced Vibration, 2nd. ed., Van Nostrand Reinhold, NY (1990)
[2] Chr. Heck & F. Ohle, submitted to Phys. Rev. E (1995)
[3] Hübler & Lüscher, Naturwissenschaften **76**, 67 (1989)
[4] F. Ohle, M. Welge & A. Hübler, Proc. of 12.Symp. on Turbulence, edt. X.Reed, A11 (1990)

Helv Phys Acta
Vol. 68 (1995)

0018-0238/95/020217-02$1.50+0.20/0
(c) Birkhäuser Verlag, Basel

Deterministic noise amplification

C. W. Heck and F. Ohle

Institut für Angewandte Mechanik und Strömungsphysik der Universität Göttingen,
Bunsenstr. 10, 37073 Göttingen, Germany

Temporal pattern learning, control, prediction and time series analysis share a common problem: deducing optimal equations of motion from observation of time-dependent behavior. In this work we describe how a dynamical system can strongly amplify stochastic influences initiated from the external environment. We will illustrate that local instabilities in state space cause fluctuations to be temporarily amplified, even though the deterministic motion is quite stable when averaged over the long term.

It is well known that low dimensional models can be constructed from experimental time series [1] if certain requirements are fulfilled, the most important one being that the series can be embedded in a low dimensional state space. For experimental systems the influence of noise on this representation is of considerable interest. It has been shown by Deissler and Farmer [2] that a dynamical system can strongly amplify stochastic influences initiated from the external environment without generating "noise" of its own accord and that local instabilities in state space cause fluctuations to be temporarily amplified. As an example a trajectory of the van der Pol equation $dx/dt = \dot{x} = -y$ and $\dot{y} = \epsilon(1-x^2)y + x + \sigma_N \eta_N(t)$ with $\epsilon = 0.5$ and an additive noise term $\sigma_N \eta_N$ is presented in Fig. 1. Here $\eta_N(t)$ describes uncorrelated gaussian white noise with a mean of zero and a variance of one and σ_N the amplitude of the noise. Fig. 1 shows that the width of the limit cycle depends significantly on the location in state space, showing regions of larger and smaller noise amplification. In the following it will be illustrated how the knowledge about noise amplification helps to explain the apparent complexity of measurement data.

A velocity time signal $x(t)$ of a resonantly stimulated von Kármán vortex street at $Re = U_\infty d/\nu = 190$ (U_∞: flow speed, d: cylinder diameter, ν: kinematic viscosity) is considered [4]. Measurement data embedded in a two dimensional time derivative state space are shown in Fig. 2. The data $x(t)$ have been normalized to an average of zero and an amplitude of about one. A polar coordinate system $[\alpha, r(\alpha)]$ with its origin in $[x = 0, \dot{x} = 0]$ is introduced for description. It has been shown elsewhere [3] that the signal can be accurately described by a low dimensional model of the type

$$\ddot{x} = \frac{d^2x}{dt^2} = \sum_{\substack{i=0,\dots,3 \\ j=0,\dots,3-i}} a_{ij}\, x^i\, \dot{x}^j. \tag{1}$$

The trajectory has the form of a limit cycle with a considerable width that is described by the standard deviation $\sigma(\alpha)$ of the experimental data from their mean cycle $\bar{r}(\alpha)$ (Fig. 3). Figure 3 suggests the existence distinguished angle dependent structure in state space.

Therefore the question arises, if this structure is resulting from the stochastic environmental influences acting on the system, as described for numerical systems [2], or caused by

the projection of a higher dimensional deterministic dynamical system onto the two dimensional plane. To examine this point, a model of type (1) describing the average trajectory $\bar{r}(\alpha)$ was constructed from the experimental data (for details see Ref. [3]). This model reproduces the average limit cycle and the physical behavior of the data very accurately. Now the above introduced additive noise term is added to the model equation, yielding

$$\ddot{x} = \sum_{\substack{i=0,\dots,3 \\ j=0,\dots,3-i}} a_{ij}\, x^i\, \dot{x}^j + \sigma_N\, \eta_N(t). \tag{2}$$

Fig. 4 shows the standard deviation $\sigma(\alpha)$ of the distance of a trajectory from equation (2) from the average cycle $\bar{r}(\alpha)$ as a function of the angle α for $\sigma_N = 0.06$. A close qualitative agreement with the experimental data in Fig. 2 is found. This implies the conclusion that the experimental system can indeed be described by a two dimensional deterministic system perturbed by gaussian white noise and thus is an experimental observation of deterministic noise amplification.

References

[1] J. Cremers and A. Hübler, Z. Naturforschung **42a**, 797 (1987)
[2] R.J. Deissler and J.D. Farmer, Tech. Rep. LA-UR 89-4236, Los Alamos Nat. Lab. (1989)
[3] C.W. Heck and F. Ohle, submitted to Phys. Rev. E (1995)
[4] F. Ohle, to appear in Chaos, Solitons and Fractals (1995)

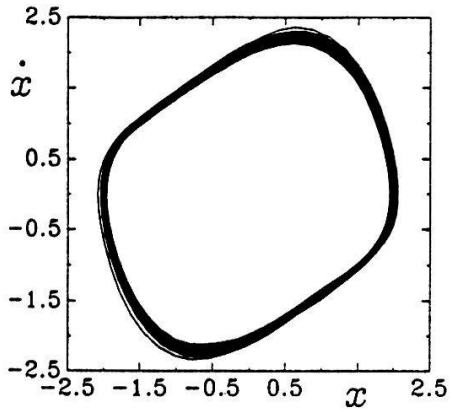

Fig. 1: State space reconstruction of a van der Pol oscillator with additive dynamical noise

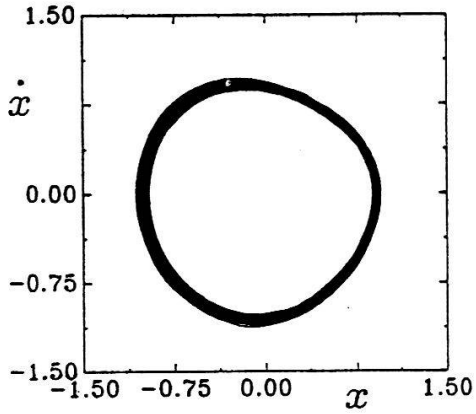

Fig. 2: State space reconstruction from experimental data of a vortex street at $Re = 190$

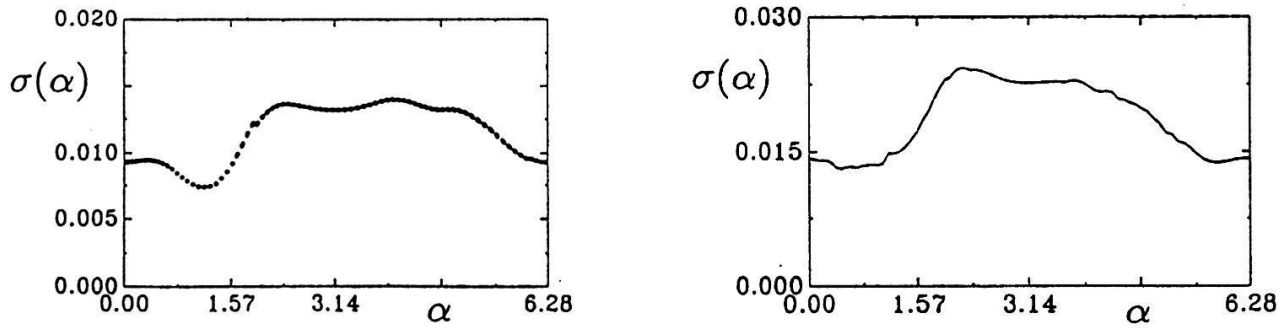

Fig. 3: Variance $\sigma(\alpha)$ of the distance of the actual trajectory $r(\alpha)$ from the average limit cycle $\bar{r}(\alpha)$ of the experimental data (left) and as simulated by Eq. (2) (right)

Helv Phys Acta
Vol. 68 (1995)

0018-0238/95/020219-02$1.50+0.20/0
(c) Birkhäuser Verlag, Basel

ELEMENTARY GEOMETRIC FIGURES IN FULLY DEVELOPED TURBULENT PLANE POISEUILLE FLOW

P.W. Egolf

Swiss Federal Laboratories for Materials Testing and Research, CH-8600 Dübendorf

D.A. Weiss

Laboratoire d'Aérothermique du C.N.R.S., F-92190 Meudon, France

A completely analytical theory of plane turbulent Poiseuille flow has been derived. In this article the infinite Reynolds number solutions, describing fully developed turbulent flow - which can be described by a rectangle, a semi-circle and two triangles -, are presented and compared with experimental data.

When the difference-quotient turbulence model was published [1], F. Busse proposed to test the new closure scheme also on turbulent shear flows along walls. Taking three important fundamental fluid dynamic problems into consideration (see Fig. 1), it was decided to first solve the plane turbulent Poiseuille flow.

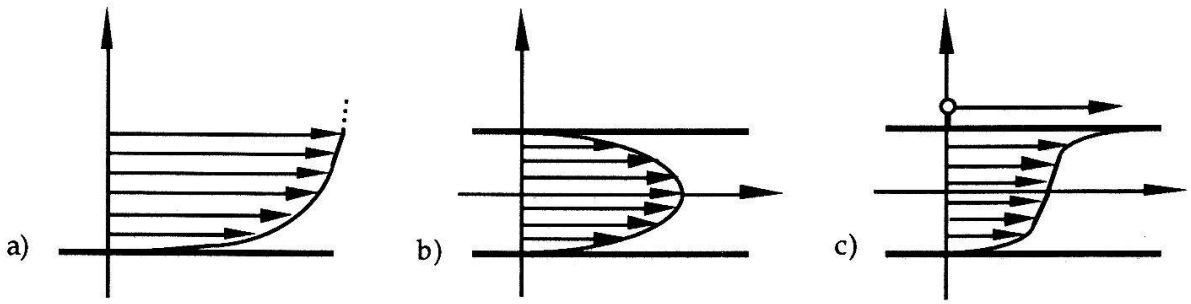

Figure 1: The time-averaged velocity profiles of different "wall"-turbulent shear flow problems: the flow along a single wall with a semi-infinite flow region (a), the symmetric plane Poiseuille flow (b) and the antisymmetric plane Couette flow between two plane parallel plates (c).

Because of symmetry arguments only one Reynolds equation has to be considered. By scaling and similarity approaches the partial differential equation is transformed to an ordinary one of Riccati type

$$\alpha \cdot \eta \cdot g_1'(\eta) - \beta \cdot g_1(\eta) + \beta \cdot g_1(\eta)^2 + \eta^2 = 0 \,. \tag{1}$$

The mean flow velocity field g_1 and Reynolds shear stress $g_{2,1}$ have been scaled and η denotes a dimensionless distance from the center line of the two plane parallel plates. The boundary condition and the Reynolds shear stress are

$$g_1(1) = 0, \text{ respectively } \qquad g_{2,1}(\eta) = \beta \cdot \frac{1}{\eta} \cdot g_1(\eta) \cdot [1 - g_1(\eta)] \,. \tag{2}$$

The solutions for moderate Reynolds numbers Re are represented by rational functions of Bessel functions of the first type. Furthermore relations between the order of the Bessel functions, the parameters α, β and Re are obtained. In this overview only the two simple limiting cases can be discussed.

1) Laminar flow: $\alpha = \frac{1}{2}$, $\beta = 0$: (3)

$$g_1'(\eta) = -2 \cdot \eta \quad \Rightarrow \quad g_1(\eta) = 1 - \eta^2 \text{ and } \quad g_{2,1} = 0 . \tag{4}$$

This is the parabolic mean velocity profile of laminar plane Poiseuille flow.

2) Fully developed turbulent flow: $\alpha = 0$, $\beta = 4$:

$$g_1(\eta)^2 - g_1(\eta) + \frac{1}{4}\eta^2 = 0 \quad \Rightarrow \quad g_1(\eta) = \frac{1}{2} \cdot \left(1 + \sqrt{1 - \eta^2}\right) \text{ and } \quad g_{2,1} = \eta . \tag{5}$$

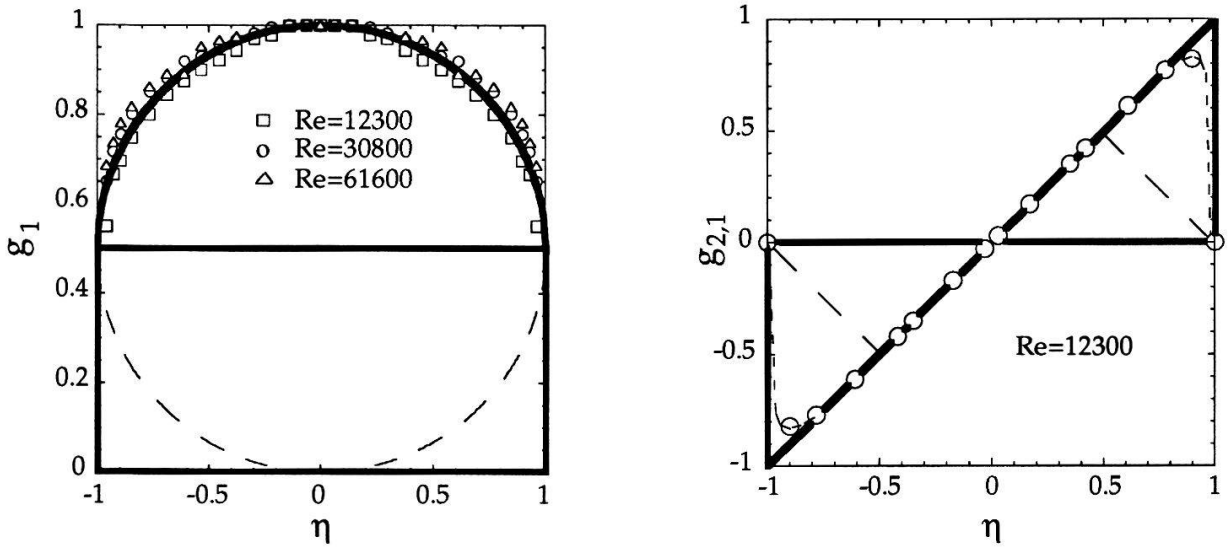

Figure 2: Comparison of theoretical results with experimental data. The mean velocity profile can be described by a semi-circle added to a rectangle (on the left), and the Reynolds shear stress is composed by two twisted triangles shown on the right-hand side.

The solutions of equation (5) are compared with experimental results from Ref. [2] and are shown in Fig. 2. Because of the elementary nature of the results the mass flow can be derived by means of simple geometrical formulas.

A more detailed presentation of the theory is in preparation.

[1] P.W. Egolf, 1994, Difference-quotient turbulence model: a generalization of Prandtl's mixing-length theory, Phys. Rev. E **49 (2)**, 1260-1268.

[2] J. Laufer, 1950, Some recent measurements in a two-dimensional turbulent channel, J. of Aeronaut. Sci., 277-287.

Helv Phys Acta
Vol. 68 (1995)

0018-0238/95/020221-02$1.50+0.20/0
(c) Birkhäuser Verlag, Basel

Oberflächenionisation in Raumfahrtsexperimenten

M.R. Aellig, P. Wurz und P. Bochsler
Physikalisches Institut, Universität Bern, Sidlerstr. 5, 3012 Bern

Durch die Anwendung der laborerprobten Oberflächenionisation in Satellitenexperimenten können niederenergetische Neutralteilchen *in situ* massenspektrometrisch analysiert werden. Durch die Reflexion an einer Oberfläche mit geringer Austrittsarbeit können die Teilchen negativ geladen werden. Erste Messungen unter Vakuumbedingungen, die ungünstiger als die Bedingungen auf einer Raumsonde sind, zeigen, dass ein cäsiumbeschichteter Wolframeinkristall die Erzeugung von Anionen während mehr als einem Tag ermöglicht. Nebst den hohen Ionisationseffizienzen von bis zu 30% für H_2 bietet der geringe Leistungsbedarf dieser Ionisationsmethode einen weiteren Vorteil.

Der Bedarf eines hocheffizienten Ionisationsverfahrens (Ionisationswahrscheinlichkeit $> 10^{-2}$) für niederenergetische Neutralteilchen (10 – 300 eV) niedriger Flussdichten ist bei vielen aktuellen Fragen der Raumforschung evident, denn erst die Ionisation erlaubt eine massenspektrometrische Analyse dieser Teilchen. Die *in situ* Bestimmung des D/H-Verhältnisses und der weiteren Zusammensetzung des interstellaren Neutralgases kann wichtige Hinweise auf die Frühgeschichte des Universums und des Sonnensystems geben. Eine weitere Anwendung ist die Fernerkundung von magnetosphärischen Plasmen durch die Analyse von Plasmateilchen, die durch Ladungsaustausch mit exosphärischem Gas neutralisiert werden. Die Neutralteilchen werden durch Reflexion an einer Oberfläche niedriger Austrittsarbeit negativ geladen. Die mit einer Atomlage Cäsium beschichtete W(110)-Oberfläche hat eine Austrittsarbeit von $\Phi = 2.15$ eV. Die Energie des Affinitätszustands der zu untersuchenden Teilchen wird durch das Bildladungspotential des Metalls verringert. Nahe der Oberfläche wird der in der Energie verbreiterte Affinitätszustand durch tunnelnde Metallelektronen besetzt. Trifft ein Kation auf die Oberfläche, so wird es vorgängig neutralisiert. Der Ladungszustand vor der Reflexion ist also unwesentlich für die Effizienz des Umladungsprozesses. An den reflektierten Anionen kann mit einem Massenspektrometer eine Massen- und Energieanalyse vorgenommen werden. Die Raumfahrtstauglichkeit der Oberflächenionisation ist direkt mit der Zeitabhängigkeit der Konversionseffizenz unter dem Einfluss von Restgaskontaminationen verknüpft. Eine Oberflächenrekonditionierung mit thermischer Desorption des Cäsiums und der Restgasadsorbate vom Substrat und anschliessender Bedampfung mit Cäsium sollte nicht mehr als zweimal pro Tag vorgenommen werden müssen. Mit dem in Abb. 1 schematisch dargestellten Experiment wurde die Umladung von H_2 an einer Cs/W(110)-Oberfläche untersucht.

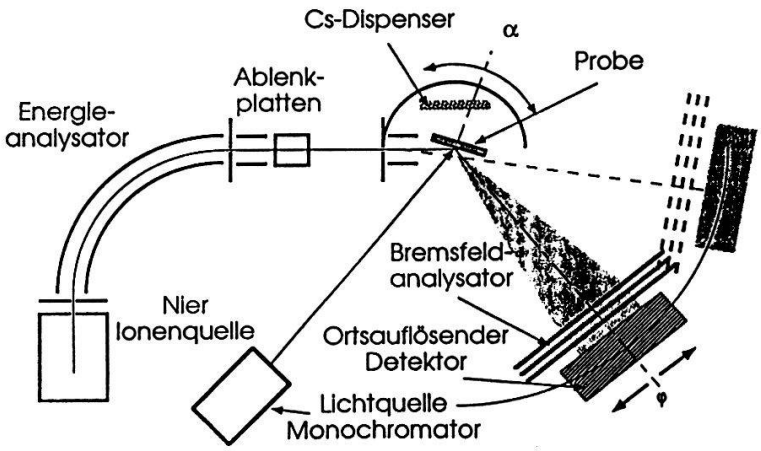

Abb. 1: Schema des Experimentes

Der Strahl besteht nach der Reflexion aus H_2 und H_2^- und wird mit einem zweidimensional ortsauflösenden Detektor untersucht. Mit einem Bremsfeldanalysator kann die negative Fraktion ausgeblendet werden, wodurch die Ionisationseffizienz und die Energieverteilung der negativ geladenen Teilchen berechnet werden können. Das H_2^--Ion ist nicht stabil und hat eine mittlere Lebensdauer von 10^{-5} sec [1]. Da die Ionen aber etwa 10^{-6} sec nach ihrer Entstehung nachgewiesen werden, ist der Einfluss der Instabilität sehr gering. Aus der Energieverteilung der Ionen kann geschlossen werden, dass die Moleküle bei der Reflexion nicht aufbrechen. Die Austrittsarbeit Φ wird photoelektrisch gemessen. Sie dient als Mass für die Oberflächenverunreinigung. In Abb. 2 ist die zeitliche Entwicklung der Austrittsarbeit und der Ionisationseffizienz eingezeichnet. Daraus wird die hervorragende Bedeutung der Austrittsarbeit für die Konversionseffizienz ersichtlich.

Bei einer Teilchenenergie von 225 eV und einem Einfallswinkel von 80° beträgt die Ionisationseffizienz 14%. Selbst nach einem Tag Restgasexposition bei einem Druck von 10^{-7} torr liegt die Ionisationseffizienz mit 2% weit oberhalb der Effizienz von Elektronenstossionisation. Da der Druck in einem Satellitenexperiment um mindestens eine Grössenordnung kleiner ist als in diesem Laborexperiment, wird eine Rekonditionierung etwa alle 10 Tage notwendig sein. Der Anstieg der Austrittsarbeit und die damit einhergehende Abnahme der Ionisationseffizienz ist durch die Anlagerung von Restgas bedingt. Für eine Strahlenergie von 100 eV wurden Effizienzen bis 30% gemessen. Der mittlere Leistungsbedarf des Ionisationsverfahrens liegt in der Grössenordnung von 0.01 – 0.1 Watt und erfüllt damit eine weitere Randbedingung für satellitengestützte Experimente.
Eine detailliertere Diskussion der Resultate ist in [2] zu finden.

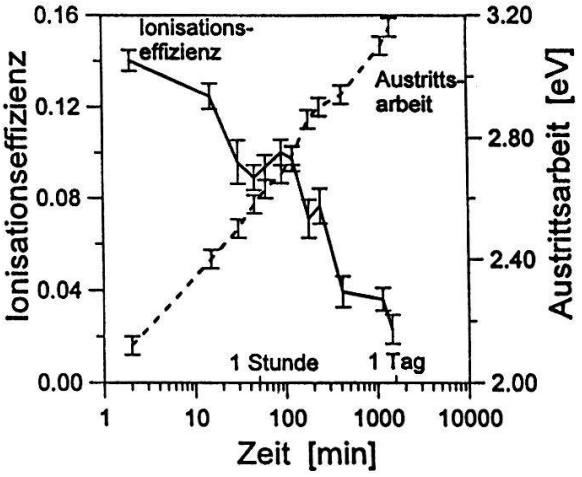

Abb. 2: Ionisationseffizienz und Austrittsarbeit in Abhängigkeit der Expositionszeit.

Referenzen

[1] W. Aberth et al., Phys. Rev. Lett. 34,1600 (1975).
[2] M.R. Aellig, Lizentiatsarbeit, Universität Bern (1995).

Helv Phys Acta
Vol. 68 (1995)

0018-0238/95/020223-02$1.50+0.20/0
(c) Birkhäuser Verlag, Basel

Optimization Study for a Measurement of Polarization Observables in μ^-–Capture on Nuclei

R.Abela[2], K.Bodek[1,4], P.Böni[2], F.Foroughi[2], L.Grenacs[3], L.Jarczyk[4], St.Kistryn[1,4], J.Lang[1], R.Müller[1], S.Navert[1], O.Naviliat-Cuncic[1], A.Proykova[6], J.Smyrski[4], J.Sromicki[1], E.Stephan[1,5], A.Strzałkowski[4], J.Zejma[4], W.Zipper[5]

1 Institut für Teilchenphysik, Eidgenössische Technische Hochschule, Zürich, Switzerland
2 Paul Scherrer Institut, Villigen, Switzerland
3 Institut de Physique Nucléaire, Université Catholique de Louvain, Louvain-la-Neuve, Belgium
4 Institute of Physics, Jagellonian University, Cracow, Poland
5 Institute of Physics, University of Silesia, Katowice, Poland
6 Institute of Physics, University of Sofia, Bulgaria

The experiment is aimed at a precise determination of the induced pseudoscalar form factor F_P in μ^--capture on ^{16}O nuclei via a measurement of the polarization observables P_{av}, P_L and T_2^0. The method uses the β-decay asymmetry as an analyzer of the spin orientation of the produced ^{16}N nuclei. Several tests were performed in order to find optimal conditions for measurement with stack targets, sensitive to the recoil direction of the ^{16}N nuclei. In addition the possibility of measuring P_{av} using of a water–based target has been investigated.

The high momentum transfer in muon capture on nuclei makes this process sensitive to induced couplings difficult to access in β-decay. Particularly interesting is the induced pseudoscalar form-factor F_P which can be used to test a variety of QCD motivated models predicting scaling laws for nucleon and meson masses, the pion decay constant and the pion-nucleon coupling constant in nuclear media [1,2]. The experiment proposed to be performed with a polarized muon beam from the Ring Cyclotron of Paul Scherrer Institute [3] aims to determine F_P in the $\mu^- +^{16} O \rightarrow^{16} N_{gs} + \nu_\mu$ reaction. In this investigation time-even correlations, ie. longitudinal polarization P_L, average polarization P_{av} and alignment T_2^0 of the residual ^{16}N nuclei are of interest. The experimental method is based on the stack target technique, sensitive to the ion-recoil direction. The β-decay of ^{16}N is used as spin orientation analyzer. The polarization of muons stopped in the target is determined from auxiliary measurement with use of the time integrated method of muon spin rotation in a slowly varying magnetic field, the so called Hanle method. First tests were devoted to optimization of the experimental conditions with respect to background and measurement of muon induced β-activities in various materials.

The long lifetime of ^{16}N (10.3 s) allows to separate the activation unit from the well shielded detection system (β-polarimeter) where β-decay electrons are registered. The activation unit is equipped with a muon energy degrader, a plastic scintillator as a beam monitor and a muon polarization monitor. A mechanical target transport system moves the target together with the spin holding Helmholz coils between the activation unit and β-polarimeter. In this way the target can be kept constantly in a field holding a nuclear spin throughout the phases of activation, transport and β-decay measurement. The β-polarimeter consists of two symmetric VETO-ΔE- E plastic scintillator telescopes arranged in tight geometry. It is shielded with about 5cm of brass and massively with light materials. In later tests two BGO crystals for γ-detection were placed above the telescopes in an appropriate opening in the shield.

An easy to use and very well suited medium for muon capture on ^{16}O is water. Thus a water target has been used to optimize the background conditions. Measurements of room and beam-correlated background were performed with the target at activation position. With a massive shielding of light materials and the use of a beam chopper a signal-to-background ratio 50:1 has been achieved.

The recoil direction sensitive target is a stack consisting of trilayers. The production layer, in our case an oxide, is sandwiched between polarization destroying (D-layer) and polarization retaining (P-layer) material where recoiling ^{16}N are implanted. The potential layer materials had to be tested and chosen with respect to muon induced β-activities which could obscure the investigated transition and influence thereby the measured β-decay asymmetry. Tests were performed

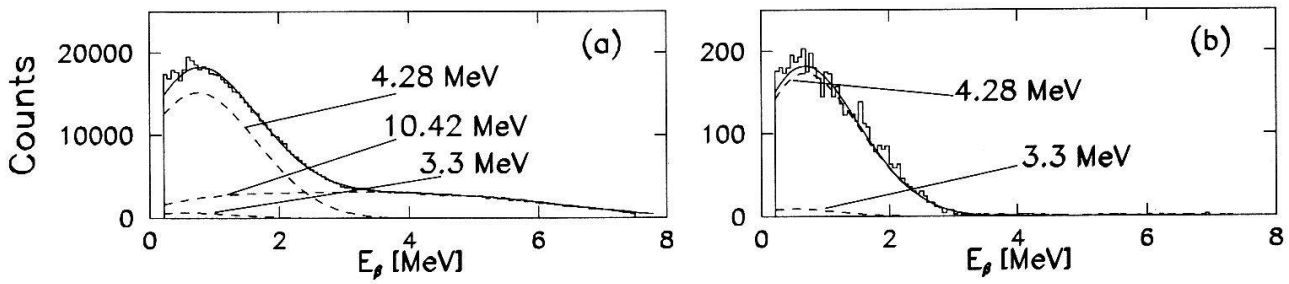

Figure 1: Spectra collected with water target decomposited into β-transitions (endpoints energies indicated): a) - single β-spectrum b) - β-γ-coincidence spectrum gated by $E_\gamma \geq 4$ MeV.

for energies up to 10 MeV and decay times ranging between 1 and 60 s. The spectra taken with an Al-target (candidate for D-layer) exhibit two β-transitions with maximal energy of about 6.7 and 4.4 MeV and decay times of 1.6 s and 54.2 s, respectively. They were identified as originating from the reactions ^{27}Al(μ,p)^{26}Na and ^{27}Al(μ,α)^{23}Na. Similarly, other metals as Cu, Ag and Pd (potential D-layer) reveal significant muon induced β-activities with energies up to 3 MeV.

A unique chance to suppress all kinds of electron background is given by the fact that the interesting $^{16}N \rightarrow^{16} O_{3+}$ (E_{max} = 4.28 MeV) transition is followed by deexcitation of ^{16}O with emission of 6.1 MeV γ-quanta. A β-γ-coincidence condition with requirement that deposited $E_\gamma \geq 4$ MeV reduced the contaminant β-activities very effectively. For palladium a suppression factor of 10^3 was achieved. Simultanously this condition allowed to reject the $^{16}N \rightarrow^{16} O_{2-}$ (E_{max} = 10.42 MeV) transition from β-decay of ^{16}N - see fig.1.

Furthemore, the possibility to measure P_{av} alone using the target containing water with an admixture of NH_4Cl was studied. At the University of Louvain the polarization relaxation time of ^{14}N in such solutions was measured by means of NMR. Expected relaxation time for ^{16}N polarization obtained with the spin/quadrupole moment scaling formulae is between 4 and 8 s and should still be increased by heating of the solution [4]. We performed a series of measurements activating with the muon beam different water solutions of NH_4Cl heating the target up to 60° C. Measurements with and without spin holding field (13 mT) were alternated in order to cancel systematic errors. However, within the experimental accuracy ($\leq 5 \cdot 10^{-3}$) the observed β-decay asymmetry is consistent with zero. Upper limit for ^{16}N polarization relaxation times T_1 is about 3 s for concentration 375 g/cm^3 and saturated solution. A possible source of discrepancy between expected and measured T_1 could be attributed to the low holding field. Another explanation could be failure in the used theory of physicochemical processes.

Our setup was optimized for measurement of the nuclear polarization produced in muon capture reaction on ^{16}O. In the tested materials the significant muon induced contaminant β-activities were found. The β-γ-coincidence technique with appropriate γ-energy threshold solves this problem and opens the way for wide class of materials to be used in the stack targets. Therefore a new β-polarimeter arangement is under preparation in which a γ-detection system consisting of 64 BGO detectors covering roughly 70% of the full solid angle will be incorporated. In the water-based target a fast polarization relaxation of the residual nucleus was observed. Thus in the next tests a stack target with few hundreds trilayers cooled to about 20 K (in a movable cryostat) will be investigated.

References

[1] M. Lutz, S. Klimt, W. Weise: Meson properties at finite temperature and barion density, University of Regensburg, Report No. TPR-91-12.

[2] L. Grenacs: Ann. Rev. Sci. **35** (1985) 455.

[3] M. Allet et al.: PSI Proposal R-93-03.

[4] L. Grenacs, A. Proykova: private communication